UNIVERSIDAD COMPLUTENSE DE MADRID

FACULTAD DE CIENCIAS FÍSICAS

Máster en Astrofísica

TRABAJO DE FIN DE MÁSTER

Modelado de Schwarzschild para el estudio dinámico de galaxias externas con MEGARA en el Gran Telescopio Canarias

Schwarzschild Modeling for the Dynamical Study of External Galaxies with MEGARA on the Gran Telescopio Canarias

Andrés Beamuz Mingote

Supervisado por:

Armando Gil de Paz

Curso académico 2024-2025

Convocatoria de septiembre

Calificación: 9.9

Contents

1 Introduction **2**

2 Methods **3**
- 2.1 Schwarzschild orbit-superposition method . . . 3
- 2.2 Stellar population synthesis . . . 3
- 2.3 Signal to noise ratio . . . 3

3 M32 observations, data reduction and post-processing **4**
- 3.1 Observations . . . 4
- 3.2 Data reduction . . . 5
- 3.3 Post-processing . . . 5
  - 3.3.1 Cubes astrometry calibration . . . 5
  - 3.3.2 Kinematic calibration with overlap regions . . . 6

4 Data analysis **9**
- 4.1 pPXF . . . 9
- 4.2 Kinematic maps . . . 10
- 4.3 DYNAMITE implementation and models optimization . . . 12
  - 4.3.1 Input data and format . . . 12
  - 4.3.2 Running the software . . . 13
  - 4.3.3 Optimization process . . . 13
  - 4.3.4 Orbit library configuration and computational cost . . . 14
  - 4.3.5 Uncertainty ranges and model to data deviations . . . 16

5 Simulation results **16**
- 5.1 Kinematic maps . . . 16
- 5.2 Viewing angles . . . 18
- 5.3 Triaxiality . . . 19
- 5.4 Supermassive central black hole . . . 20
- 5.5 Orbit type classification . . . 20

6 Discussion and conclusion **23**

A Appendix I. Kinematic pointing calibration implementation **24**

B Appendix II. Simulation results after imposing symmetry on h3 kinematic map **24**

Resumen

Presentamos nuevos modelos dinámicos de la galaxia elíptica compacta M32 basados en espectroscopía de campo integral de alta resolución con MEGARA. Utilizando el método de superposición de órbitas de Schwarzschild, obtenemos una masa central de agujero negro supermasivo (SMBH) de $(3.6^{+0.2}-0.1) \times 10^6$ M$\odot$, consistente con estimaciones previas pero con incertidumbres significativamente menores. Nuestros modelos favorecen una inclinación más baja ($\theta = 46.0^{+0.3^\circ}-0.5$) que la propuesta en trabajos anteriores, lo que implica que M32 es intrínsecamente más achatada ($q = 0.44^{+0.06}-0.04$) y más soportada por rotación de lo que se pensaba. La dependencia radial de los cocientes de ejes y de la triaxialidad indica además la presencia de un componente fino similar a un disco interno.

La descomposición orbital muestra que aproximadamente un $\sim 15\%$ de las estrellas ocupan órbitas calientes y otro $\sim 15\%$ órbitas contrarrotantes, firmas dinámicas que apuntan hacia factores externos. Estas características ayudan a reafirmar que la estructura actual de M32 fue moldeada por encuentros con M31, que incluyeron efectos de marea y flujos de gas que probablemente alimentaron la formación estelar nuclear. En conjunto, nuestros resultados proporcionan la descomposición orbital más detallada de una galaxia elíptica compacta hasta la fecha, ofreciendo nueva evidencia de que este tipo de galaxias pueden formarse a través de la interacción entre una concentración intrínseca (previa a la interacción) y procesos ambientales externos.

Palabras clave: galaxias: cinemática y dinámica—galaxias: individual: M32—galaxias: formación—galaxias: evolución—métodos: análisis de datos

Abstract

We present new dynamical models of the compact elliptical galaxy M32 based on high-resolution MEGARA integral-field spectroscopy. Using Schwarzschild orbit-superposition methods, we obtain a tightly constrained central SMBH mass of $(3.6^{+0.2}_{-0.1}) \times 10^6$ $M_\odot$, consistent with previous estimates but with significantly reduced uncertainties. Our models favor a lower inclination ($\theta = 46.0^{+0.3^\circ}_{-0.5}$) than earlier works, implying that M32 is intrinsically flatter ($q = 0.44^{+0.06}_{-0.04}$) and more rotationally supported than previously thought. The radial dependence of axis ratios and triaxiality further indicates the presence of a flattened nuclear disk-like component.

The orbital decomposition shows that roughly $\sim 15\%$ of stars occupy hot orbits and another $\sim 15\%$ counter-rotating orbits, dynamical signatures that point towards external factors. These features help reaffirm the case that M32's present structure was shaped by encounters with M31, including tidal stripping and gas inflows that likely fueled nuclear star formation. Taken together, our results provide the most detailed orbital decomposition of a compact elliptical to date, offering new evidence that such galaxies can arise from the interplay between intrinsic compactness (prior to interaction) and external environmental processes.

Key words: galaxies: kinematics and dynamics—galaxies: individual: M32—galaxies: formation—galaxies: evolution—methods: data analysis

1 Introduction

On scales above ~ 200, Mpc, the Universe is homogeneous and isotropic, but at smaller scales it is structured into galaxy groups, clusters, and filaments. In this regime, galaxy formation and evolution are strongly influenced by environmental processes—tidal interactions, mergers, ram-pressure stripping, and similar mechanisms—collectively referred to as "nurture." By contrast, the "nature" scenario attributes galaxy properties primarily to internal processes and initial conditions at formation. Distinguishing between these two pathways requires disentangling their signatures, and the most powerful way to do so is through dynamical studies, since the orbital structure and mass distribution of a galaxy retain the clearest record of its assembly history.

The gravitational potential of a galaxy is formed by the mass of its stars, gas, dark matter, and central supermassive black hole (SMBH). The Schwarzschild orbit-superposition method provides a flexible, non-parametric way—does not assume a specific functional form for the distribution function—to infer these components by fitting observed kinematics with superpositions of stellar orbits. This technique has been extensively applied to study SMBHs, intrinsic shapes, and orbital structures across all galaxy types [36, 38, 39].

Over the last two decades, large integral-field spectroscopic surveys such as ATLAS 3D [10], CALIFA [29], SAMI [4], MaNGA [5], and MASSIVE [25] have revolutionized our understanding of galaxy dynamics. By providing spatially resolved line-of-sight velocity distributions (LOSVDs), these surveys have revealed systematic trends in galaxy structure, including connections between stellar populations, angular momentum, and environment. In contrast to these large surveys, this work focuses on high-resolution (in this work $R \sim 12000$) MEGARA [21] observations with the Gran Telescopio Canarias (GTC), whose $R \sim 6000$–20000 spectral resolution and fine spatial sampling allow for precision dynamical modeling of Local Group galaxies.

Among the population of elliptical galaxies, compact ellipticals (cE) remain poorly understood in part because they are extremely rare. Although they exhibit high central surface brightness, their small sizes and low overall luminosities make spatially resolved spectroscopy challenging. Their frequent proximity to massive galaxies suggests a capture and tidal truncation origin [13]. M32, the closest cE galaxy to the Milky Way (MW), is a natural laboratory for studying this process, given its location near the massive spiral M31—a dominant member of the Local Group. Early dynamical studies with HST and ground-based IFUs detected a central SMBH with a mass of $\sim (2-3) \times 10^6$ $M_\odot$ and a close to oblate shape [36, 39]. Intriguingly, this SMBH is comparable in mass to that of the much larger Milky Way, suggesting that either M32 has suffered a significant structural evolution or, alternatively, that SMBHs can form and grow under very different circumstances, ultimately residing in galaxies with dramatically different properties.

Evidence indicates that M32 is not a simple elliptical galaxy but a tidally transformed remnant of a larger progenitor. Simulations by [3] propose that M32 originated from the tidal stripping of a low-mass early-type spiral by M31, losing its outer disk and halo while triggering central star formation through gas inflows. In [19] it is similarly argued that M32 is the stripped core of a spiral galaxy that merged with M31 roughly 2 Gyr ago. In contrast, [18] suggests that tidal stripping alone cannot fully explain the properties of M32, favoring an intrinsically compact progenitor. These studies collectively highlight the complexity of cE formation, with additional roles proposed for AGN feedback and gas depletion.

This work aims to provide new constraints on the internal structure and assembly history of M32 using high-resolution MEGARA observations. Through orbit-based Schwarzschild modeling, we derive its central black hole mass, intrinsic shape, orbital structure, and dark matter contribution, offering new insight into its origin and the evolution of compact ellipticals.

This work is structured as follows: Section 2 introduces the methods and techniques later implemented. Section 3 describes the observations, data reduction, and calibration. Section 4 presents the extraction of stellar kinematics, analyzes the Gauss-Hermite moments maps, and concludes with obtaining the best-fit model. Section 5 discusses the resulting dynamical model. Finally, Section 6 summarizes our findings and compares them to existing dynamical results and hypotheses for the formation of M32 as it is observed today.

2 Methods

This section introduces the three key methodologies employed in this work. First, we describe the already mentioned Schwarzschild orbit-superposition method for constructing dynamical models of galaxies. Next, we present the theoretical basis for deriving stellar kinematics from integral field unit (IFU) data via stellar population synthesis (SPS) modeling. Finally, we present the importance of achieving a uniform signal-to-noise ratio (S/N) in the data and its role in kinematic calibration and binning.

2.1 Schwarzschild orbit-superposition method

The Schwarzschild orbit-superposition method [32] is a flexible dynamical modeling technique used to reconstruct the mass distribution and internal structure of galaxies and stellar systems. Starting from a parametrized surface brightness distribution, typically described with a Multi-Gaussian Expansion (MGE; [20]), the luminosity is deprojected to infer the intrinsic mass density given an assumed set of viewing angles and a gravitational potential that may include contributions from dark matter or a central black hole [37]. In this potential, a large library of representative stellar orbits is integrated numerically, sampling the full phase space to avoid biases from missing orbit families. The method then determines non-negative orbital weights that best reproduce the observed surface brightness and stellar kinematics. By exploring parameter space, Schwarzschild modeling allows for robust constraints on the mass-to-light ratio, dark matter content, black hole mass, viewing geometry, and the internal orbital structure of the galaxy [36].

2.2 Stellar population synthesis

The light we observe from a galaxy is the combined emission of all its stars, each contributing according to its intrinsic spectrum, age, metallicity, and chemical composition. In order to derive the LOSVD we have to broaden their combined spectrum and then fit it. In this work, Stellar Population Synthesis (SPS) is used to extract stellar kinematics from IFU observations of M32. SPS is a method to interpret this integrated light by modeling it as a combination of simpler stellar populations [34, 15]. Each simple stellar population (SSP) represents a coeval group of stars with a single age and metallicity, and an assumed initial mass function (IMF). By fitting a set of SSP templates to the observed spectrum, one can infer the stellar content, star formation history, chemical enrichment, and stellar kinematics of the system. SPS relies on extensive libraries of SSP models covering a range of ages, metallicities, and, in some cases, abundance ratios. It is important that the instrumental resolution of the templates (their intrinsic σ) is equal to or lower than that of the observations in order to accurately recover all kinematic components.

2.3 Signal to noise ratio

Achieving a high and uniform signal-to-noise ratio (S/N) across the field of view is essential for extracting reliable stellar kinematics and population parameters from IFU data. Spectra with low S/N can bias velocity and dispersion measurements, as well as age and metallicity estimates, while excessively high S/N in some

regions may lead to unnecessary oversampling. To address this, the data are spatially binned to a target S/N, ensuring that each spatial bin contributes equally reliable information to the dynamical modeling.

3 M32 observations, data reduction and post-processing

In this section, the data observed from M32 are first described. Then, the data reduction process is summarized, along with a precise description of post-processing, which includes adjusting each pointing astrometry data using PNe and a higher spatial resolution HST image, and calibrating the kinematic maps using the overlap regions between different pointings.

3.1 Observations

The observations of M32 used in this work were obtained in September 2018 with the 10.4-m Gran Telescopio Canarias (GTC) at the Observatorio del Roque de los Muchachos, La Palma, using the optical integral-field spectrograph MEGARA [21]. Each pointing consists of a set of five frames with equal exposure time of 540 s under the open time program GTCMULTIPLE4A-18B. The central pointing was observed on commissioning (August 2017) with five frames of 600 s of exposure time. Standard calibration data—including bias and dark frames, flat fields, and arc-lamp exposures—were also acquired. Table 1 summarizes the key observational parameters, including the instrument mode, grating, spaxel size, spectral coverage, and resolving power. The table also lists the field of view (FoV) for individual and combined pointings, the exposure time per frame, the spatial configuration of pointings, and the coordinates of each pointing (RA and Dec).

To study the resulting orbital structure, nine (see Table 1 for spatial disposition) MEGARA Integral Field Unit (IFU) pointings were acquired around the central regions of M32. This extended the effective field of view from approximately 100 arcsec^2 to 900 arcsec^2, significantly improving spatial coverage at the expense of increased complexity in data reduction and analysis.

Observational Setup		**Pointing Information**				
Quantity	Value	Pointing	RA (J2000)	Dec (J2000)	Date	Seeing [arcsec]
Instrument mode	LCB	OB00-0	00:42:41.83	40:51:55.0	08/27/17	1.0
Grating	VPH521-MR	OB00-1	00:42:40.80	40:51:55.0	09/05/18	1.0
Spaxel size (hex.)	$0.62''$	OB00-3	00:42:40.80	40:52:05.8	09/08/18	1.0
Spectral range	4963–5443 Å	OB00-4	00:42:41.83	40:52:05.5	09/07/18	0.9
Resolving power	$R \sim 12{,}000$	OB00-5	00:42:42.87	40:52:05.8	09/08/18	1.0
Resampled pixel size	$0.4'' \times 0.4''$	OB00-6	00:42:42.87	40:51:54.9	09/06/18	1.1
Single pointing FoV	$12.5'' \times 11.3''$	OB00-7	00:42:42.87	40:51:44.0	09/08/18	0.9
Pointings disposition	3×3	OB00-8	00:42:41.83	40:51:44.2	10/01/18	0.7
Combined FoV	$\sim 36.4'' \times 34''$	OB00-9	00:42:40.80	40:51:44.2	10/01/18	0.8

Table 1: MEGARA setup and pointing coordinates with observation dates for the M32 dataset.

RA (J2000)	Dec (J2000)	Morphological Type	Distance [Mpc]	$R_{\rm eff}$ [arcsec]	$\mu_{\rm central}$ [mag/arcsec^2]
$00^{\rm h}42^{\rm m}41.8^{\rm s}$	$+40°51'55''$	cE2	0.77	30	12.65

Table 2: Basic properties of the galaxy M32. Position, morphological type, distance, effective radius, central surface brightness, and radial velocity are listed (see [23, 24, 26, 27]).

3.2 Data reduction

In this subsection, we describe the data reduction process. The data were reduced by Armando Gil de Paz and Mario Chamorro Cazorla using the MEGARA Data Reduction Pipeline (DRP), first introduced by [28], and following the procedures outlined in [11] and [12]. For each pointing, the final data product is a `final_rss.fits` file, where each row contains a fully flux- and wavelength-calibrated spectrum corresponding to a single spaxel.

The reduction begins with bias removal, overscan correction, and trimming to match the detector size. During this step, bad pixels are also masked using a reference file provided with the pipeline. Dark frames are not required for MEGARA, as the instrument produces only < 2 e^-/h/px. Wavelength calibration is performed using arc-lamp exposures taken during the same night as the science frames, except for pointings #8 and #9 (see Figure 2), for which calibration frames from other adjacent nights were used. Since each MEGARA fiber behaves as an independent system with its own wavelength response, the DRP corrects these variations using fiber flat-field images. Flux calibration is performed using measurements of the spectrophotometric standard stars HR1544, HR7950, and BD12237. Each of these steps produces correction files that are subsequently applied to the raw data. Before applying these corrections, the presence of diffuse light is evaluated and accounted for when necessary. However, this was not deemed necessary in the case of these observations.

At this stage of the data reduction process, the computed calibration and correction files are applied to the observations. Sky subtraction is performed using the spectra from the outermost fibers of the MEGARA MOS. It is worth noting that at the wavelengths covered by the MR-G grating, no prominent sky emission lines are detectable at the exposure times used, which prevents correcting the wavelength calibration using sky lines. Additionally, although the sky bundles (56 fibers) are located 1.7–2.4 arcmin from the IFU center, they still capture light from the faint outskirts of M32 and the disk of M31. Fortunately, the surface brightness in these regions is negligible compared to the central IFU field (sampled by the 567 fibers of the Large Compact Bundle (LCB)). This full reduction procedure was applied to all nine MEGARA pointings covering the central regions of M32.

3.3 Post-processing

In this subsection, we outline the post-processing steps applied to the reduced data to prepare the final inputs for the Schwarzschild simulations. Three key procedures are performed: (1) Data-cube generation, (2) re-calibration of the astrometry for each data cube to correct positional offsets, and (3) kinematic re-calibration based on the overlap regions between adjacent pointings.

For subsequent processing, the data were resampled from the native hexagonal spaxels to a Cartesian grid with square pixels. This transformation, carried out via interpolation, simplifies handling the data and also allows it to be treated in the simulation software (see Section 4.3.1). During this resampling, the pixel size was changed from $0.62''$ to $0.4''$, requiring interpolation between the original spaxels.

3.3.1 Cubes astrometry calibration

In principle, telescope control systems place each IFU pointing at pre-specified sky coordinates. However, mechanical flexure, thermal expansion, pointing errors, and weather fluctuations during each observation night can introduce systematic shifts in position, particularly in fiber-fed instruments like MEGARA. While wide-field imaging datasets allow straightforward correction via registration against a deep reference image, IFU datasets from MEGARA present additional challenges due to their small field of view and lower spatial resolution. The GTC website reports that the astrometric accuracy of the telescope is on the order of 1–2 arcsec. Following a procedure similar to that in [12], we performed an astrometry validation. Upon visual inspection of the uncorrected data (Figure 1a), it became evident that the astrometric alignment across the nine MEGARA cubes was inaccurate.

To correct for these offsets, PNe detected through the [O III] λ5007 Å emission line (blueshifted to $\sim$ 5002 Å in M32) as precise spatial anchors were used. Each MEGARA cube was aligned to an archival HST/WFC3 F502N image (exptime=600 s) from program ID 11714 (PI: Howard E. Bond) ([33]), convolved to approximate ground-based seeing ($\sim$ 0.5 arcsec). By slicing the cubes at the [O III] wavelength and identifying matching PNe, we computed relative RA and Dec shifts between the cubes and the HST frame.

Figure 1b shows the result after applying these astrometric corrections. The pointings now overlap seamlessly, and no significant spatial gaps remain. One cube (pointing #9) did not contain visible PNe, making this

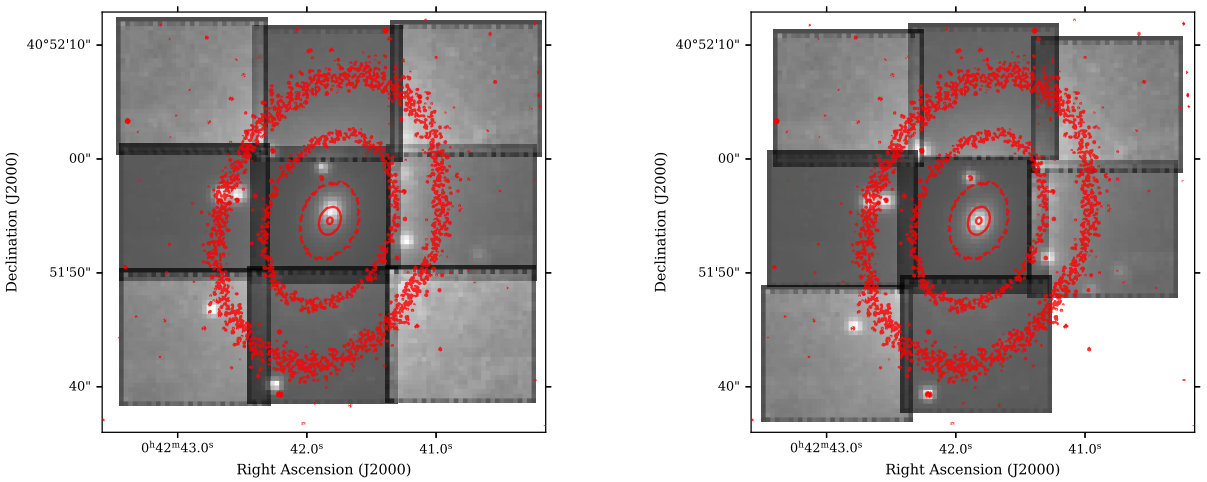

(a) Before astrometry correction.

(b) After astrometry correction.

Figure 1: Summed wavelength cube slices near the [OIII] emission line overlaid with the *HST* ground-seeing degraded image before and after the astrometry correction. On the left panel, the PNe seen in the MEGARA observations do not match those of the *HST*. After the correction, as shown on the right panel, every PNe matches the position on the *HST* image. Note that using this axis orientation, North points upwards, and East to the left. The discrepancy in background gray intensity between each pointing is caused by summing differing quantities of wavelength slices and how bright in the designated spectral range each PNe is.

method unusable for that pointing. As shown in Figure 6 of [12], the astrometric error is systematic and likely caused by a time-dependent pointing drift that increases with the delay (typically ~ 1 minute) between correcting the pointing position and locking onto the guide star. For pointing #9, we therefore adopted the mean offset computed from the other eight pointings.

The distribution of individual RA and Dec corrections is summarized in Table 3. The RA offsets cluster around ΔRA mean ~ 0 arcsec, while the Dec offsets show a consistent southward shift of approximately ΔDec mean ~ -1 arcsec. Note that Figure 1 follows the standard astronomical convention: RA increases to the left (E), and Dec increases upward (N).

Following astrometric realignment, the individual data cubes were merged into a single cube which is also referred as hypercube. To minimize interpolation artifacts and ensure clean overlap between pointings, the outer spaxels of each cube were slightly trimmed, yielding fields of 31×27 square pixels per pointing. The final mosaic, shown in Figure 2, illustrates the spatial coverage, the origin of the data for each pixel, and the pointing identifiers assigned during acquisition. The resulting hypercube spans 91×85 pixels (see Table 1 for combined field of view), with pointings hereafter referred to by their figure labels (e.g., pointing #0 denotes the central field).

The fill color in each rectangle indicates which pointing contributes the displayed data in regions of overlap, reflecting the stacking order adopted during mosaic construction. The figure also highlights overlap regions, as well as small gaps where no pointing provides coverage. Pixels in uncovered areas remain empty. Notably, pointings #7 and #8 share a common border but, due to trimming, their edges meet exactly without overlapping pixels.

Where multiple pointings cover the same pixel, only one cube contributes data, following the defined stacking hierarchy. These overlap regions and their impact on the final kinematic maps are further discussed in Section 3.3.2, where a calibration scheme ensures a consistent and harmonized kinematic solution across the full field.

3.3.2 Kinematic calibration with overlap regions

Combining the nine astrometry-corrected cubes into a single *hypercube* effectively creates a dataset resembling a single-pointing observation of M32 with MEGARA, but with a much larger field of view while preserving the native spatial resolution of the instrument.

Using this hypercube, we derived kinematic maps for the first four Gauss–Hermite (GH) moments by applying

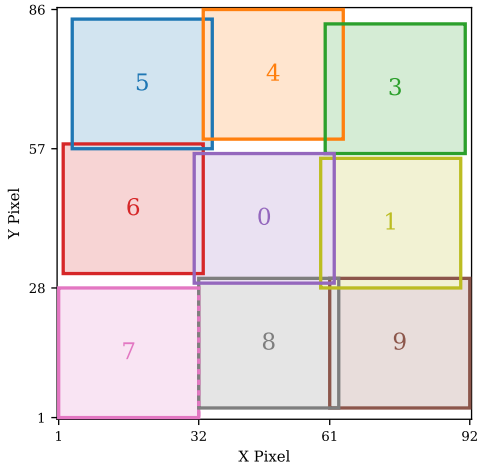

Figure 2: Final spatial distribution and labeling of the 9 pointings used to create the data hypercube. The labels correspond to the OB00-i of Table 1. The different coloring is used to indicate on the overlap regions to which pointing the data on that pixel belong to.

Pointing	ΔRA [arcsec]	ΔDec [arcsec]
OB00-0	0.18	-0.90
OB00-1	0.90	-1.44
OB00-3	0.90	-1.44
OB00-4	-0.84	0.18
OB00-5	-0.90	-1.08
OB00-6	0.07	-0.54
OB00-7	0.81	-1.48
OB00-8	-0.54	-0.79
OB00-9	0.07	-0.94

Table 3: Offsets for RA and Dec in arcsec for each OB00-i pointing. The label for each pointing corresponds to the distribution shown in Figure 2. Pointing #9 is corrected using the mean displacement from the rest.

two methods introduced earlier: (1) Voronoi binning to achieve approximately uniform signal-to-noise ratio of 30 (see Section 2.3), and (2) SPS modeling with `pPXF` (see Section 2.2). The resulting maps are shown in Figure 3 and are analyzed in detail in Section 4.2.

Although these maps capture the overall structure of the kinematics of M32, noticeable discontinuities appear at the boundaries between pointings, particularly in the velocity and h_4 maps. Correcting these mismatches is essential because Schwarzschild models are designed to reproduce smooth and symmetric stellar dynamical structures.

The discrepancies between pointings are primarily driven by variations in instrument focus and temperature, which affect the shape of the Line Spread Function (LSF). This limitation arises because the top-level requirements of the instrument specify resolving power but not strict control over LSF symmetry. Additional small velocity offsets may also arise from instrument flexure or minor inaccuracies in the heliocentric correction. Moreover, the spectral range of the MR-G grating lacks bright sky lines that could be used for an independent post-processing calibration. As a result, the overlap regions between adjacent pointings provide the only robust way to empirically recalibrate their relative kinematics.

We developed a custom calibration scheme to homogenize the GH moments across pointings. The procedure designates one pointing (A) as a reference and calibrates an adjacent pointing (B) by matching their kinematic measurements in the overlap region, then propagating the correction across the full field. For example, pointing #5 was chosen as a reference to calibrate pointing #4 through their shared region. In this framework, the reference pointing and the one being calibrated are consistently referred to as A and B, respectively.

For each overlap, we re-extracted the four GH moments (V,σ,h_3,h_4) and their uncertainties using `pPXF` (Section 4.1) without previously applying the Voronoi binning. Any observed mismatch is attributed to slight variations in the instrumental LSF, which we model as a convolution effect. The derivation of the calibration equations is detailed in Appendix A. A kernel-based convolution approach was initially explored but rejected, as it produced large deviations from the data. Instead, we developed an analytic expansion of the line-of-sight velocity distribution (LOSVD) in terms of its GH moments, yielding algebraic equations that relate differences in σ, h_3 and h_4 between pointings. These equations were then applied in a chained calibration process, beginning with pointing #0 (selected for having the highest S/N) and propagating corrections along three chains: [0–6–5–4–3], [0–8–9], and [0–1].

We tested three variants of this method, introducing small variations to how we implement the aforementioned equations:

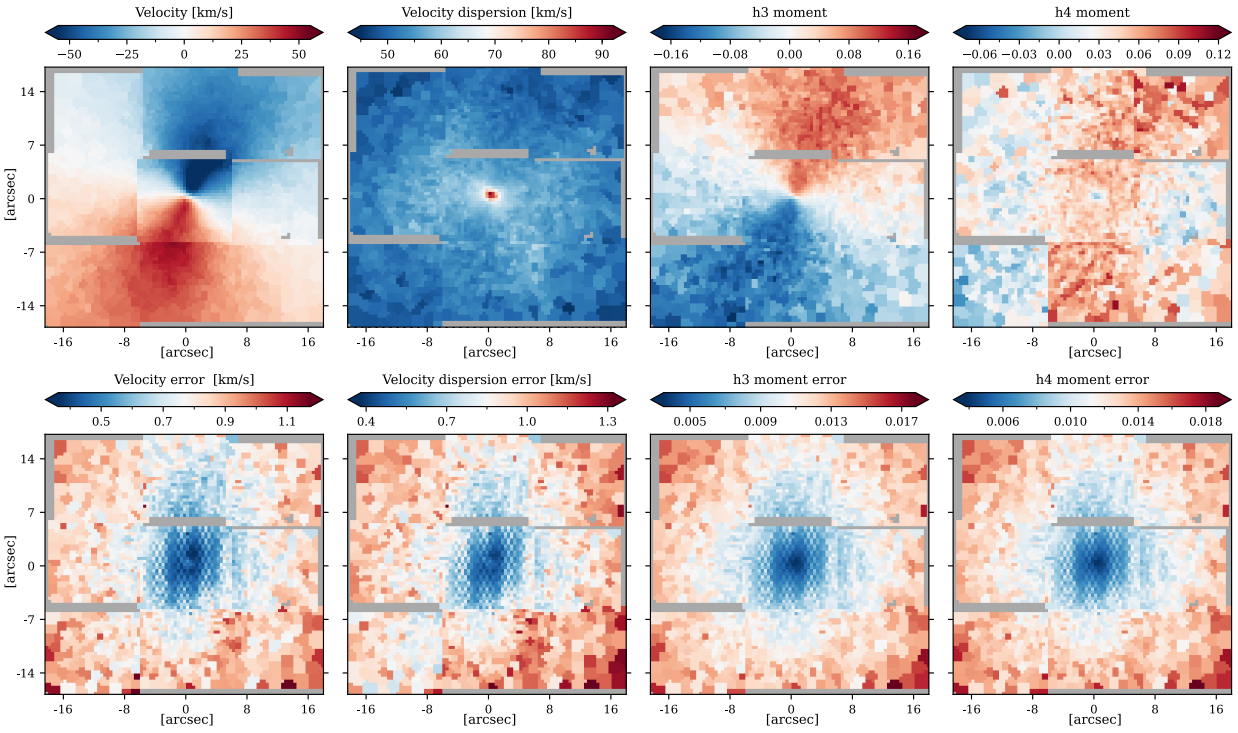

Figure 3: Kinematic maps for the first four GH moments on the first row and their error maps on the second after applying the astrometry correction to the reduced data. The axes show angular distance from the center. Gray pixels mean no data available. The kinematic correction is explained and discussed in the text.

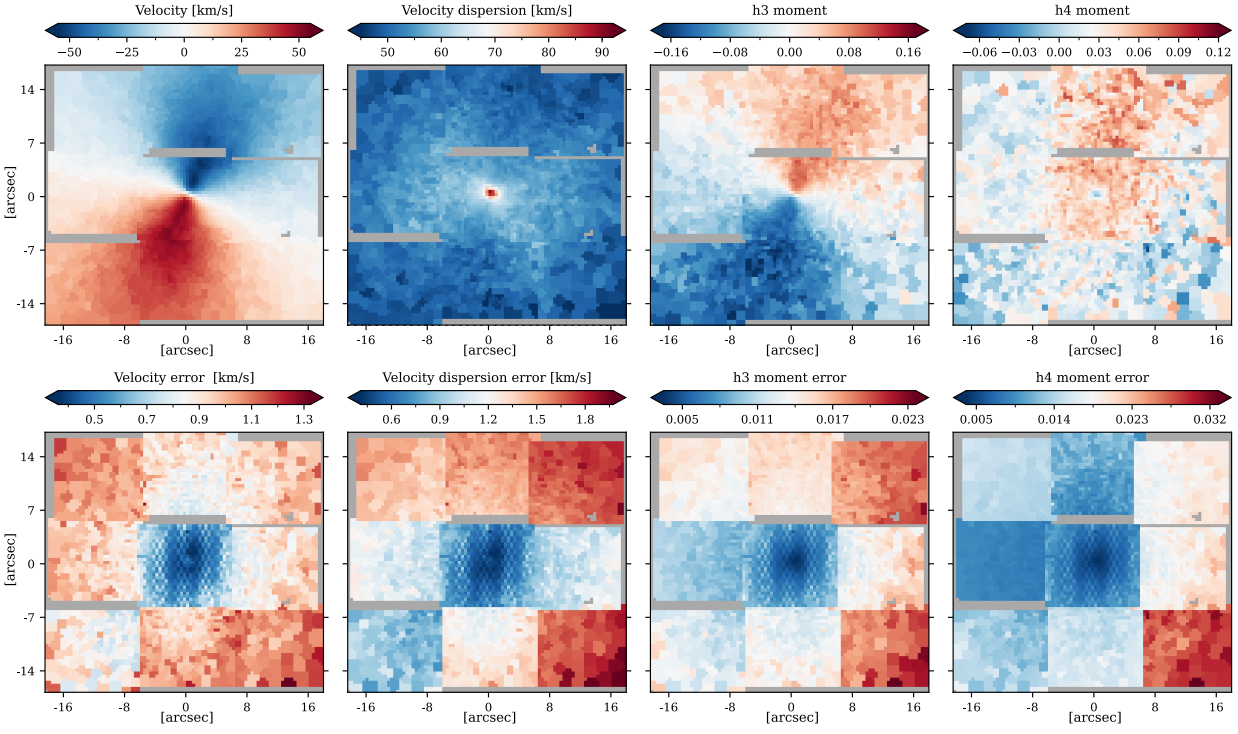

Figure 4: Kinematic maps on the first row and their error maps on the second after applying the kinematic calibration using the overlapped regions and the third describe method for the overlap region calibration. Note the difference in error due to the uncertainties in the kinematic re-calibration. The errors' increment follow the chain sequences applied.

1. Pixel by pixel correction using the specific σ_B value of each pixel on the corrected pointing.
2. Pointing mean correction, using the mean value of each pointing $\overline{\sigma_B}$ to adjust h_3 and h_4.
3. A combination of the second method with mean values for σ_B with leaving h_4 in pointing #4 unchanged (as seen on the original Coelho map 3) and correcting pointing #3 with the original #4 being the reference. Same for pointing #9, corrected with the original pointing #8.

While all three methods worked for the velocity, velocity dispersion and h_3, methods 1 and 2 strongly distorted h_4 in pointings #4 and #3. Methods 1 and 2 increase the sharp step between pointings #5 and #4 as the overlap values of h_4 differ substantially. The σ values derived from the overlap region between pointings #0 and #8 are sufficiently big to distort pointing #8 if corrected. Hence, we adopted method 3 to be used for the kinematic calibration between pointings.

The resulting kinematic maps are shown in Figure 4. Transitions between pointings are smooth, especially in velocity, though a positive excess in h_4 persists in pointings #4 and #3, breaking the radial symmetry. We note that this lack of radial symmetry on the h_4 map might be real, e.g., caused from stars in M32 or even from the disk of M31. The h_3 map also shows reduced amplitude in the positive sign region. These residuals and their physical implications are discussed in later sections. Note how, due to the spaxel to cube interpolation process, the initial error maps visible in Figure 3 follow a Moiré pattern.

4 Data analysis

In this section, we analyze the fully post-processed data. Section 4.1 details the application of the `pPXF` method to extract stellar kinematics from our MEGARA observations, comparing results obtained with two different stellar population libraries. Section 4.2 examines the resulting kinematic maps through radial and circular slices and compares V/σ diagnostics with previous surveys. Lastly, Section 4.3 introduces the `DYNAMITE` software package, which we use to model the internal structure of M32 and recover its orbital distribution.

4.1 pPXF

The methodology for extracting stellar kinematics via stellar population synthesis (SPS) is introduced in Section 2.2. In this work, we apply it to integral field spectroscopy (IFS) of M32 obtained with MEGARA. We use the Penalized Pixel-Fitting method (`pPXF`) to fit simple stellar population (SSP) model templates to each spatial bin and measure the LOSVD and its higher-order GH moments. This widely used technique was first presented in [9], extensively refined in [7], and most recently reviewed in [8].

Combining the astrometry-corrected hypercube with a stellar library and `pPXF` fitting yields spatially resolved kinematic maps. Our initial fits employed the empirical MILES library [30], which consists of ~ 1000 stellar spectra observed with the 2.5-m INT telescope. MILES covers the range λ3525–7500 Å at a resolution of 2.3 Å. However, its empirical nature limits the parameter space coverage, especially for non-solar abundances, and its relatively narrow wavelength range can restrict its applicability. As mentioned earlier (see Section 2.2), the spectral resolution of the template library must be equal to or higher than that of the instrument used; otherwise, the recovery of all kinematic components may be compromised (does not happen with MILES in this case).

To address the MILES limitations, we used the theoretical Coelho library [14]. The high-resolution version covers λ2500–9000 Å at 0.02 Å resolution, offering a wide parameter space with both solar and α-enhanced abundance compositions. Its synthetic design provides complete coverage of stellar atmospheric parameters, allowing fits to a wider range of stellar populations. The main drawback is that its flux calibration is theoretical rather than tied to observed spectrophotometry, which may require empirical corrections for precise stellar population synthesis. These corrections though should have minor impact on the kinematic analysis.

The Coelho-based kinematic maps derived from the astrometry-corrected hypercube are shown in Figure 3. Applying the overlap-based kinematic calibration described in Section 3.3.2 yields the final maps in Figure 4. These corrected maps show substantial improvement over both the MILES-based results and the uncalibrated Coelho maps: the discontinuities between pointings are smoothed out, the saturation of higher-order moments is resolved, and small-scale kinematic structures are recovered at higher fidelity.

4.2 Kinematic maps

To further investigate our data we extracted four slices: two linear (along the galaxy's major and minor axes) and two circular (at fixed radii). These are shown in Figure 5. In the top panels, the linear slices are overlaid (gray along the major axis at 68° and black along the minor axis at 158°), and the circular slices are plotted for radii of 3 arcsec (black, entirely within pointing #0) and 13 arcsec (gray, spanning all eight pointings). The top-left panel also indicates the positive, counterclockwise angle measurement with a dashed line and arrow.

The second row presents kinematic moment values and uncertainties along the linear slices, plotted against radial distance from the galactic center. Along the major-axis slice (gray), velocity exhibits a classic rotation curve, and h_3 displays a corresponding antisymmetric pattern consistent with the well-known h_3–velocity anti-correlation seen in disk-like rotation (see Section 5 of [35]). While σ and h_4 are largely radially symmetric, an h_4 excess appears in pointing #4, disrupting symmetry. Along the minor-axis slice (black), both velocity and h_3 remain near zero, which is expected for the rotation axis, where symmetric LOSVDs produce negligible skewness ($h_3 \approx 0$). Again, σ and h_4 remain symmetric except for the persistent h_4 excess.

The third row shows moment values and errors along the circular slices, presented versus angular distance (in radians) from the reference line visible on the velocity kinematic map. The velocity peaks at radii of ~ 5 arcsec , and the maximum velocities occur at angles corresponding to the major axis, regardless of radius, confirming consistency with the linear slices. The velocity dispersion circular slices reveal a "butterfly" pattern: symmetric with two minima aligned with the major-axis angles. The h_3 remains approximately constant at its peak amplitude across radii, mirroring the nearly flat behavior seen in the external regions of the linear major-axis slice. Meanwhile, the h_4 slices show a pronounced excess near an angular distance of $\pi/2$, along the positive major axis at both radii. Its persistence across multiple pointings, and over varying radii, strongly suggests this is a genuine physical feature. However, this will be thoroughly discussed in Appendix B.

In Section 5 of [35], the authors present a comprehensive analysis of how the higher-order moments (h_3,h_4) scale with the dimensionless rotation parameter, V/σ, across both hydrodynamical simulations with its mock IFS observations and observed data from the SAMI galaxy survey. They demonstrate that regular (fast) rotators exhibit a strong anti-correlation between h_3 and V/σ, a signature of dynamically cold, disk-like stellar components. They also show that h_3 is most pronounced along the major axis at larger radii, while h_4 reaches a minimum near the galaxy center. These patterns are commonly interpreted as dynamical evidence of past gas-rich merger events. This concurs with what is discussed in the introduction that M32 is the remnant of a past interaction between a low mass spiral galaxy and M31 [3].

Our corrected kinematic maps and slices (Figure 5) mirror these behaviors. The velocity profile clearly delineates rotation along the major axis; h_3 exhibits anti-symmetry in those regions, while both velocity and h_3 fluctuate around zero along the minor axis, as expected for the rotation axis where LOSVD asymmetry vanishes. Circular slice analyses further reinforce this picture, with velocity maxima and σ minima aligned along the major-axis angles and h_3 plateauing at peak amplitude. Moreover, relatively high h_4 values are found near the positive major axis, with a clear excess relative to the minor axis and the SE semi-major axis beyond 5 arcsec.

Furthermore, our (h_3,h_4) vs. V/σ diagrams for M32 (represented in Figure 6) place the galaxy between Classes 3 and 4 of [35], with both categories associated with fast-rotating systems containing embedded disks. This finding supports existing classifications of M32 as a compact fast rotator; indeed, [36] identifies M32 as a "nearby compact fast rotator E3 galaxy".

These results suggest that, despite the absence of a visually prominent disk in photometric observations, M32 displays robust kinematic signatures of a past gas-rich interaction, potentially with M31. Nonetheless, these conclusions are drawn exclusively from kinematic diagnostics. To derive a deeper understanding, our next step is to construct dynamical models with orbital decompositions. These models will enable us to quantitatively assess the galaxy's structural parameters and clarify the gravitational influence of M31 on M32's internal dynamics.

As noted earlier, the h_3 map is not symmetric in amplitude between the positive and negative sides. This asymmetry is evident in the linear slice along the major axis and is even more pronounced in the first panel of Figure 6, where the zero h_3 line lies clearly above the intersection between the data and the vertical line $(\mathrm{v} - \overline{\mathrm{V}})/\sigma = 0$. This effect, observed across all pointings, may be attributed to the proximity of M32 to

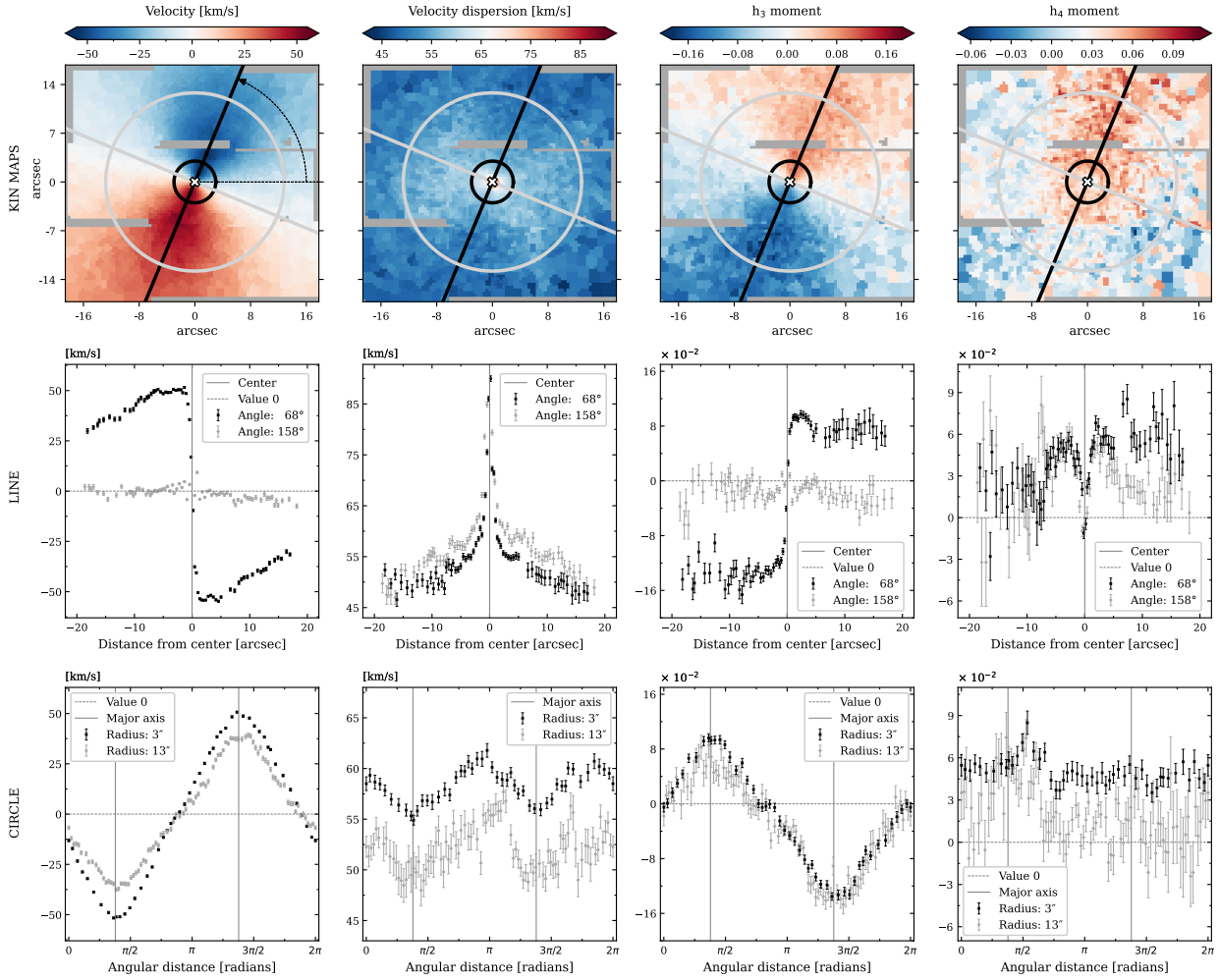

Figure 5: Corrected kinematic maps for the overlap regions, with two line and two circle slices, with directions and radius overlaid in the top row. The top-left panel also indicates the direction of positive measured angles using the thin black dashed horizontal reference line and curved arrow. The graphs on the second row show kinematic moment values (V, σ, h_3, h_4) extracted along those line slice paths, plotted against the distance from the galaxy center (marked by the white cross with a black outline on the first row). The center of the linear slice is marked with a vertical solid line. On the third row the circle slice values are shown against the angular distance from the reference line. The major axis angles (68° and 158°) are shown with a solid vertical line. On both slice types, the zero value is highlighted with a horizontal dashed line.

the much larger M31 galaxy, as well as to instrumental systematic effects. A more detailed discussion is provided in Appendix B.

Compared with previous studies of M32, such as the triaxial modeling analysis by [36] and the SAURON investigation of its intrinsic flattening and central black hole mass [39], the present dataset offers a unique combination of advantages. The observations employ a plate scale that, while not the smallest available among integral-field spectrographs, provides an optimal balance between spatial resolution and field of view. In addition, the dataset achieves a high density of spatial elements and a superior signal-to-noise ratio (up to 150 on pointing #0 and 5-10 for the outer regions per spaxel or 30 per Voronoi), the latter owing to their acquisition with the 10.4m GTC. Most importantly, the nine individual pointings cover a $\sim$ 900 arcsec^2 region, extending the spatial coverage well beyond that of earlier integral-field studies. This expanded coverage reaches regions of M32 not previously probed in dynamical simulations, enabling a more comprehensive kinematic analysis.

Adopting a distance to M32 of 0.77 Mpc (see Table 1 of [23]) and considering the angular coverage of

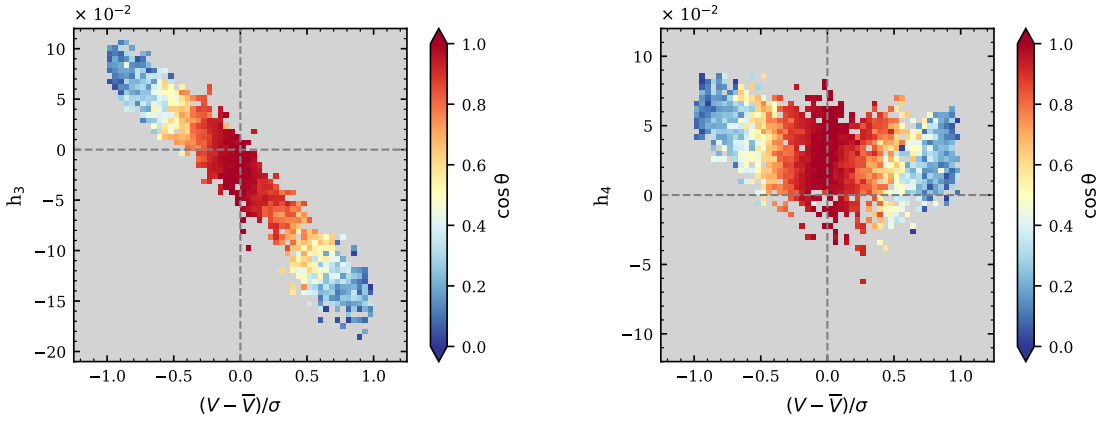

Figure 6: Skewness (h_3) and Kurtosis (h_4) vs. V/σ for our kinematic maps of M32. The color code shows the azimuthal deviation from the minor axis. As it appears in [35], regular fast rotators present a strong anti-correlation between h_3 and V/σ, and a heart-like shape for the h_4 and V/σ relation.

$36.4" \times 34"$, the resulting kinematic maps span approximately 135 pc × 126 pc. This is similar to the R_{eff} of M32 (see Table 2), meaning that approximately only half of the light of M32 is inside our observations. Due to M32's close proximity, these observations provide access to the kinematics of its innermost regions.

4.3 DYNAMITE implementation and models optimization

In this subsection, we describe the code used to construct the Schwarzschild models and the modifications applied to the data to produce the required input format. We also outline the procedure for running the code, define the model components adopted in this work, and detail the optimization process used to determine the best-fit model, including the estimation of errors and uncertainties.

4.3.1 Input data and format

The dynamical modeling was performed with DYNAMITE (DYnamics, Age and Metallicity Indicators Tracing Evolution, visited in [22]), a Schwarzschild orbit superposition code. Since the software requires square pixel sampling, the hexagonal spaxels of the original data cube were first resampled onto a Cartesian grid (see Section 3.2). To mitigate the impact of low surface-brightness regions, a target signal-to-noise (S/N) ratio of 30 is imposed, and neighboring pixels are adaptively combined until this threshold is reached, following the Voronoi binning method. Thus, each Voronoi bin achieves approximately constant S/N, except for the pixels that already had higher S/N (see Section 2.3 and 3.3.2).

As said in Section 4.1, stellar kinematics are then extracted from the Voronoi-binned hypercube using `pPXF`. The resulting kinematic maps, shown in Figure 3, illustrate the binning pattern: in the innermost, high-S/N region, most bins correspond to individual pixels, while at larger radii, multiple pixels are combined into a single bin. The centroid of each Voronoi bin is computed as the flux-weighted mean of the constituent pixel coordinates.

DYNAMITE requires a Multi-Gaussian Expansion (MGE) of the galaxy surface brightness and a kinematic table as input, both provided in specific file formats. The MGE image used in this work is an HST WFPC2 continuum observation in the F814W filter with a total exposure time of 1280 s (Program ID: 05464, PI: R. Michael Rich). In addition, a ground-based I-band image obtained with the PFCU on the 2.5-m Isaac Newton Telescope (INT), with an exposure time of 1 s, was also used for the MGE construction. Observational data are processed using a data-preparation function included with the code, which ingests the FITS table *kinematic_table.fits* and the `mge.ecsv` file. The PSF size ($\sigma_{\rm PSF}$) must also be specified to ensure that the prepared inputs match the spatial resolution of the observations. Tests show that if $\sigma_{\rm PSF}$ is overestimated, fine structures in the data may be smoothed out, reducing the sensitivity of the orbit-weight integration to small-scale features. The MGE traces the two-dimensional light distribution of the galaxy and was obtained using dedicated MGE-fitting software, see [6]. The `mge.ecsv` file contains, for each Gaussian component, its peak surface brightness [$L_\odot/pc^2$], dispersion [arcsec], observed flattening, and position angle [degrees].

The `kinematic_table.ecsv` file contains, for each Voronoi bin: projected coordinates relative to the galaxy center [arcsec], flux, line-of-sight velocity, velocity dispersion, GH moments (h_3, h_4), measurement uncertainties, and a unique bin identifier.

4.3.2 Running the software

Once the kinematic data and MGE file have been processed into the required input formats, the first dynamical simulations can be run. DYNAMITE is installed following the guide in [22]. Models are defined and executed using a configuration file in *.yaml* format, which specifies the physical parameters of the galaxy and the modeling setup.

The first section of the configuration file defines the physical parameters of the system. Basic attributes include the object name, distance [Mpc], and position angle [degrees]. The mass components of the system are then specified as a central black hole, a dark matter halo, and stars. In this work, the three components are modeled like:

- **Central Black Hole:** Modeled with a Plummer potential defined by mass (*m-bh* [$M_\odot$]) and scale length (*a-bh* [arcsec]). This prevents the numerical problems associated to the use of a point mass in the dynamical modeling.
- **Dark Matter Halo:** Described by an Navarro-Frenk-White (NFW) profile, parameterized by dark matter fraction ($f\text{-}dh = M_{200}/M_\star$) and concentration ($c\text{-}dh = R_{200}/\mathrm{NFW}_{\mathrm{length-scale}}$).
- **Triaxial Visible Component:** Represents the stellar ellipsoid derived from the MGE. It requires the intrinsic minor and intermediate axis ratios relative to the long axis (*q-star*, *p-star*), the ratio of observed to intrinsic Gaussian widths (*u-star*), and observational inputs such as the projected mass and luminosity density, as well as the kinematic maps.

After the last component is defined, the system parameter stellar mass-to-light ratio (*ml*) is specified. For every parameter you can provide either a fixed value or a range with a step. The code will use these ranges and steps to generate and simulate multiple models in a grid.

Next, the orbit library and weight solver settings are defined. The orbit library is constructed on a grid of the three integrals of motion, with grid sizes (nE, $nI2$, $nI3$). For each initial condition, three orbits are generated (one box orbit and two opposite-rotating tube orbits). A dithering parameter (*dith*) specifies the number of sub-grids around each initial condition, resulting in a total of $3 \times (nE \times nI2 \times nI3) \times dith^3$ orbits in the library. Additional parameters include the minimum and maximum radii of integration [arcsec], the orbital period sampling, and the seed (also possible to set to random) used to convolve the orbit library with the PSF.

Finally, the weight solver options and input/output directories are specified. Once the *.yaml* file is complete, the main DYNAMITE script generates the models grid, constructs the orbit libraries, integrates the orbits, and computes the orbital weights, producing diagnostic plots to evaluate the quality of the fits. DYNAMITE offers two methods for generating the models grid:

- **FullGrid**: Generates a model for every combination of parameter values, fully sampling the parameter space as defined in the configuration file. This method can become computationally expensive when exploring many parameters with fine step sizes.
- **LegacyGridSearch**: Starts from a initial model and iteratively explores the surrounding parameter space, creating new models on every iteration near the previous best-fit model. This approach is more efficient but slower per iteration and may converge to local minima if parameter step sizes are too small.

4.3.3 Optimization process

The optimization process aims to identify the model that best reproduces the observed kinematic and surface brightness data based on the chosen input parameters. The quantity minimized during optimization is the χ^2 statistic (see Section 5 of [37]), which measures the deviation of the model predictions from the observed data, weighted by the measurement uncertainties. It is defined as:

$$\chi^2 = \sum_{i=1}^{N} \left(\frac{M_i - D_i}{\Delta D_i} \right)^2, \tag{1}$$

where N is the number of Voronoi bins multiplied by the number of GH moments, M_i is the model prediction for the i-th observable, D_i is the corresponding observed value, and ΔD_i is its associated uncertainty. Lower χ^2 values indicate a better fit between the model and the data.

To compare χ^2 values across different studies, it is necessary to account for the total number of degrees of freedom (dof) in the fit. The degrees of freedom are defined as $\nu = N - p$, where p is the number of free model parameters. In this work, the final M32 dataset (see Section 4.2) contains 2326 Voronoi bins, and since four GH moments are modeled, this gives $\nu = 4 \times 2326 - 8 = 9296$ degrees of freedom, using the parameters described in the previous section. This is substantially larger than in comparable studies. For example, [31] use SAMI galaxy survey data with $\sim 10^2$ Voronoi bins, while [36] combine SAURON and STIS data for $N \sim 10^3$, both an order of magnitude smaller than in this work.

The reduced chi-square statistic is defined as $\chi^2_{\rm red} = \chi^2/\nu$ (see [31]). Ideally, a best-fit model would yield $\chi^2_{\rm red} = 1$, but this is not achievable here due to inherent limitations of the Schwarzschild method, which imposes symmetry in its solutions and therefore cannot fully reproduce asymmetric features in the data. As discussed in Section 4.2, the primary source of this asymmetry is the h_3 map. Many studies address this by symmetrizing the kinematic data (see Appendix A of [36]) to reduce noise and improve model fits. Our investigation of χ^2 minimization under symmetrization constraints is presented in Appendix B.

With the optimization statistic explained, the best-fit model search can begin. Ideally a densely populated grid of models for every parameter would be generated, but that is computationally too expensive. Thus, a more optimal parameter search must be done. First, the (p,q,u) values need to be assessed, as values too far from the real data will not allow the deprojection to converge and integrate the model. The best way to start the search, and make sure that the optimal model is not a local minimum, is doing a big grid using **FullGrid** on (p,q,u,ml) and giving fix values to the rest of the parameters.

Based on previous studies, the central supermassive black hole in M32 has close to 3×10^6 $M_\odot$. The smallest black hole scale used in DYNAMITE cannot be too small, and for starters, it is set to 0.001 arcsec. We expect the galaxy to have experienced tidal forces and other interactions with its host galaxy, M31, the Andromeda Galaxy. Those interactions seem to have depleted the external weakly bonded structures of M32, leaving only the inner regions—in agreement with its high surface brightness. Thus, the concentration is set to a high value of 10. Contrarily, the dark matter distribution may have experienced less disruption. This should lead to a much higher total-to-stellar mass ratio. The first models are set to a virial mass over stellar mass ratio of hundreds. After some big step fast iterations, the *pqu* values are set to 0.9, 0.35, and 0.95 respectively. The first parameter search iterations are used to set the initial *pqu* values. These values need to be close enough to the actual physical shape for the models to converge. The *ml ratio* is set to have a wide search range and step, as this relation can highly vary from different previous studies.

Once the first densely populated grids are integrated, a grid with higher accuracy and smaller steps is the **LegacyGridSearch**. The rest of the parameters are now freed and its optimal value is obtained after many iterations. This process appears represented in the corner plot of Figure 7, where the accuracy of each model is shown along with the complete grid used in the search. This process is accompanied by more hand-crafted searches to fill the blank spaces on the parameter search corner plot. In total, more than 2600 models have been generated and integrated, with a deprojection success rate of $\sim 85\%$.

4.3.4 Orbit library configuration and computational cost

The orbit library configuration plays a key role in the optimization process. The number of orbits must be chosen so that increasing this number further does not significantly reduce the χ^2 value. In [37], a total of $3 \times (nE \times nI2 \times nI3) = 3528$ initial orbit starting positions were adopted, with an additional dithering factor of 125, resulting in the full orbit library size. Similarly, [39] used 1960 starting positions. In this work, we increased the number of starting positions to $3 \times (23 \times 10 \times 7) = 4830$, representing a 37% and 146% increase relative to these previous studies, respectively. After extensive testing, a dithering factor of 27 was found sufficient to prevent further decreases in χ^2, providing a balance between model resolution and computational efficiency.

The DYNAMITE code solves a constrained linear least-squares problem to determine orbital weights that best reproduce the observables. Our orbit library contains $4830 \times 27 = 130{,}410$ orbits, while the kinematic maps provide ~ 9304 equations, making the system underdetermined. Positivity and optional regularization are imposed to select a physically meaningful solution. The total degrees of freedom for evaluating $\chi^2_{\rm red}$ are $\nu = 9296$, calculated as the number of observables minus the eight global model parameters. The weight

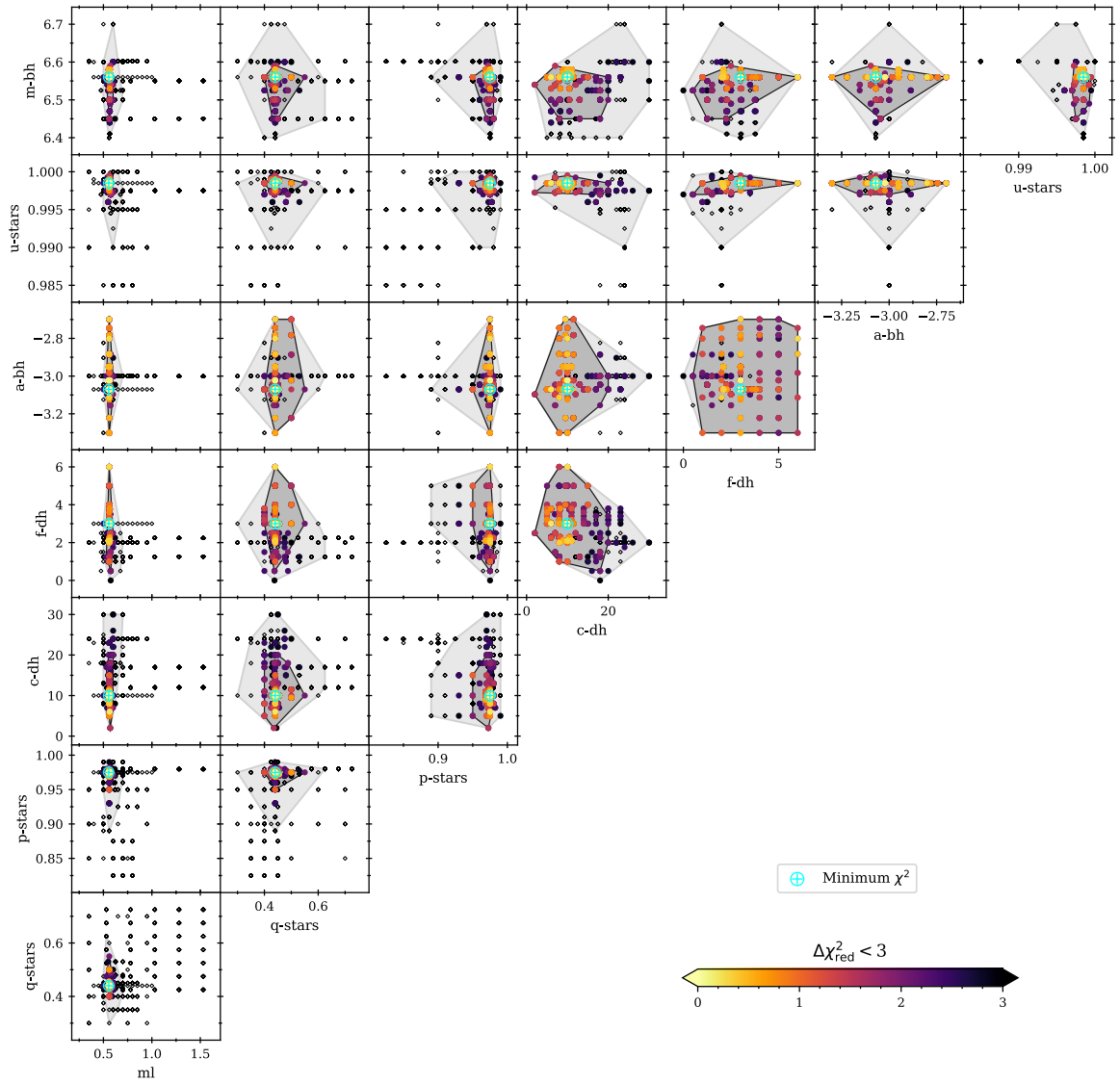

Figure 7: Corner plot of all 2614 models with integrated orbital weights. Each point represents a model, showing the values of the two parameters for the corresponding subplot axes. The color scale highlights models with $\Delta\chi^2_{\rm red} < 3$. Shaded regions indicate the 1σ (dark) and 3σ (light) confidence intervals.

solver assigns a weight to each orbit, producing a model that optimally reproduces the data under the constraints, regularization, and positivity requirements.

To perform these computations, we used four different computational environments: a personal laptop (AMD Ryzen 7 7735U CPU with 16 cores and 32 GB RAM) and three clusters: NYX, LUX, and BRIGIT. Of these, only LUX and BRIGIT proved suitable for running DYNAMITE, as NYX showed inconsistent orbit weight convergence and the personal laptop lacked sufficient memory. The final 1500 models were computed on BRIGIT, a high-performance computing (HPC) cluster at the Universidad Complutense de Madrid. BRIGIT consists of over 600 CPU cores, 3.7 TB of total RAM, and 176 TB of storage, connected through a low-latency 10 Gbps network. On BRIGIT, integration times per model dropped from $\sim$ 12 hours on LUX to $\sim$ 7 hours, and its large memory capacity enabled the simultaneous execution of multiple models, significantly accelerating the overall analysis.

The reader might wonder whether, instead of first performing a **FullGrid** search with relatively large parameter steps and then refining with a **LegacyGridSearch**, it would be feasible to construct a single **FullGrid** with fine step sizes across all parameters. However, using a step size that gives 20 discrete values for each

of the 8 parameters would require integrating 20^8 models. At ~ 7 hours per model, this would amount to several million years of computation with our current resources.

4.3.5 Uncertainty ranges and model to data deviations

Once the best-fit model is identified, parameter uncertainties are derived from the deviation of each model relative to the best-fitting solution, quantified as $\Delta\chi^2_{i-\mathrm{red}} = \chi^2_{i-\mathrm{red}} - \chi^2_{\mathrm{min-red}}$, where i indexes each model. Following [2], we adopt $\Delta\chi^2$ thresholds corresponding to 1σ, 2σ, and 3σ confidence regions, with values of $\Delta\chi^2 = 1.00, 4.00, 9.00$ for one interesting parameter ($k = 1$) and $\Delta\chi^2 = 2.30, 6.17, 11.8$ for two ($k = 2$). Figure 7 illustrates the 1σ and 3σ confidence regions for pairs of parameters ($k = 2$) in the corner plot. To estimate individual parameter uncertainties, we marginalize over the full N-dimensional parameter space ($N = 8$ in this work) and compute slices through the resulting confidence hyper-ellipsoid. No renormalization by $\chi^2_{\mathrm{min-red}}$ has been applied, meaning the minimum χ^2_{red} is not scaled to unity before deriving confidence regions. This approach, while widely used, formally assumes linear models and exact data-model agreement, which do not strictly hold for complex dynamical models [1]. Thus, the reported uncertainties provide robust constraints on the model parameters within the adopted framework, while acknowledging the limitations of applying χ^2-based confidence regions to highly non-linear systems.

In Figure 7 *m-bh*, *a-bh*, and *f-dh* are shown in logarithmic scale. The confidence contours of the corner plot also reveal which parameters strongly influence the model results. For example, small variations in *ml*, *p-stars*, *q-stars*, and *u-stars* quickly lead to large increases in χ^2, indicating these parameters are tightly constrained. In contrast, *a-bh* and *f-dh* appear to have little effect on the overall fit. The dark matter fraction relative to the stellar mass is poorly constrained because the kinematic data only extends to $r \lesssim 70$ pc. The dark halo concentration (*c-dh*) and central black hole mass (*m-bh*) do influence the fit, but the models are less sensitive to these parameters than to those defining the intrinsic galaxy shape, as reflected in their broader confidence regions.

The results of the parameter search will be analyzed in detail in Section 5.

5 Simulation results

As part of the χ^2 minimization, the best-fit model is identified. This model corresponds to the combination of input parameters that, after orbit weighting, provides the closest match to the observed kinematic maps and total flux distribution. The location of this solution is indicated by the *cyan* circle and cross in the corner plot shown in Figure 7.

In the following, this best-fit model is analyzed in detail. First, the resulting kinematic maps are compared with the observational data. The optimization yields the intrinsic shape of the galaxy as well as the viewing angles that relate the projected sky coordinates to the intrinsic configuration. Subsequently, the triaxiality and the enclosed mass profile (including the central black hole mass) are examined as a function of galactocentric radius. Finally, the orbital composition of the model is investigated, with the classification of each orbit type presented and discussed in terms of the circularity parameter λ_z and a projected orbit-type map.

5.1 Kinematic maps

After examining the χ^2 values, a fast and visually intuitive way to assess whether a model accurately represents the galaxy's dynamics is to compare the model-generated kinematic maps with the observational data and, critically, to inspect the residuals.

Figure 8 presents the kinematic and corresponding error maps of the best-fit model. The model reproduces the observed dynamics well: the overall shapes of the maps are accurately captured, particularly the velocity dispersion map, where the characteristic *butterfly* pattern is clearly recovered. The velocity and h_3 maps similarly reproduce the features observed in the data. However, discrepancies appear in the h_4 map on pointing #8, where the model produces a symmetric distribution, contrasting with the asymmetric pattern in the data (see Appendix B).

Despite the generally good match of the observed kinematic features, the error maps provide additional insight into the performance of the model. The error maps are computed as the absolute difference between the model and the data, normalized by the data uncertainty (for each pixel i, the error is $E_i = |M_i - D_i|/\Delta D_i$). The velocity error map shows larger values in pointing #0, reflecting the very small data uncertainties in

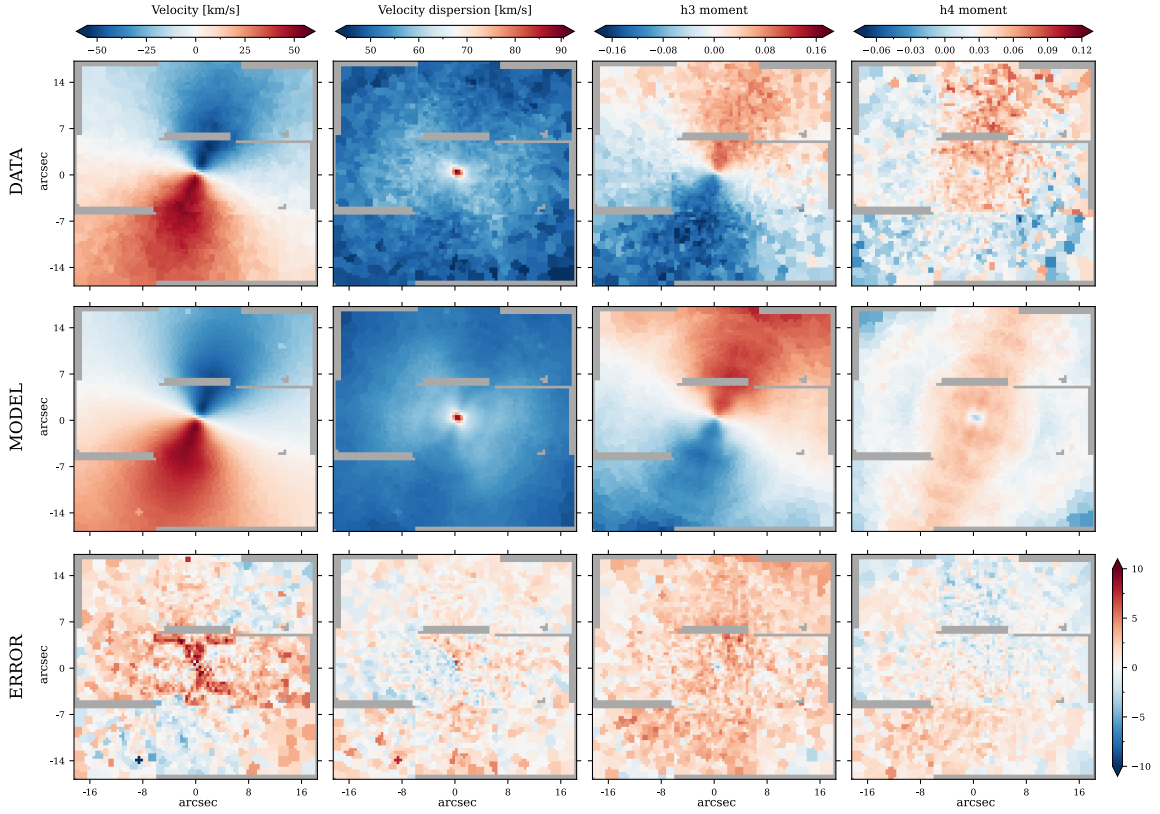

Figure 8: Kinematic maps of the data, best-fit model and residuals. As each horizontal color bar indicates, each column represents the kinematic map for the first four GH moments. The first row are the input data maps, followed on the second row by the best-fit model ($\chi^2_{\rm red} \sim 3.7$) generated maps. On the third row the residuals of the model and data are normalized with the data error maps.

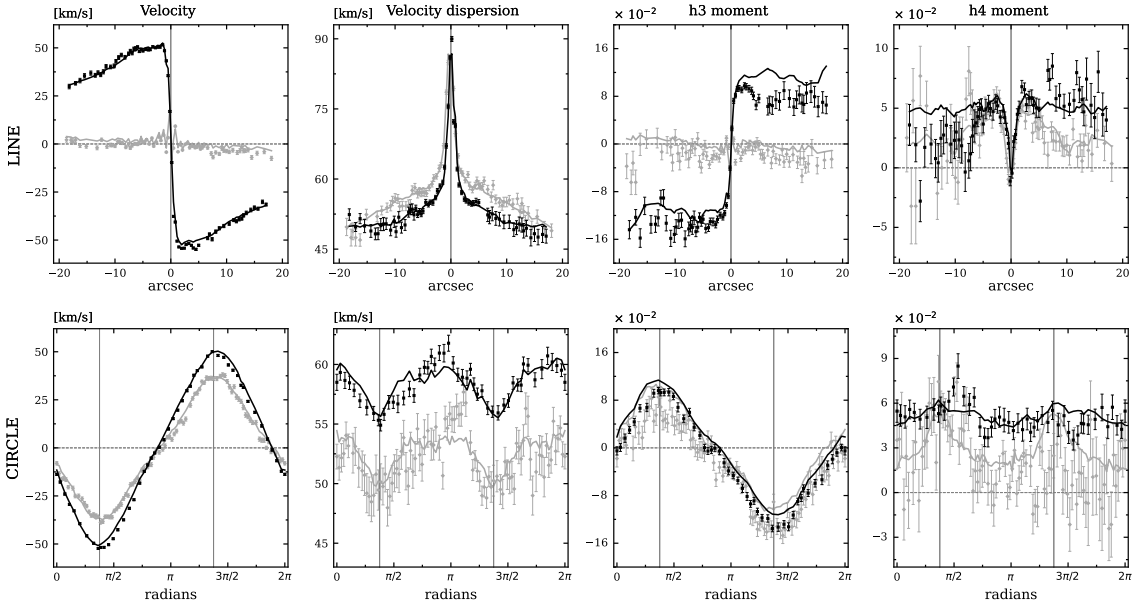

Figure 9: Scatter of data values for the linear and circular slices shown in Figure 5, along with a continuous line plot for the model results within the same slices. Same legend of the already mentioned Figure 5 applies to these slices maps.

this region. The velocity dispersion and h_4 error maps are close to zero and fluctuate around that value, indicating robust modeling. In contrast, the error map for the third kinematic moment reveals a significant discrepancy: because the model generates symmetric maps while the data are asymmetric (as discussed in Section 3), the model attempts to reconcile both sides simultaneously, resulting in an error map that is uniformly positive, highlighting the limitations of these models in reproducing the h3 map.

Figure 9 provides a more detailed comparison of the kinematic maps through the same slices defined in Figure 5. In this figure, the velocity slices of the best-fit model follow the data points with high precision. The excess of model velocity relative to the data, previously noted in pointing #0, is evident in the linear slice along the semi-major axis between 1–6 arcsec, as well as in the circular slice at small radii, particularly for azimuthal angles beyond $\pi/2$ and $3\pi/2$ radians. The velocity dispersion, on the other hand, is consistently well reproduced across the field: both the maps and the slices show excellent agreement between model and data.

The discrepancy in the h_3 map, arising from the intrinsic asymmetry of the data, becomes especially apparent in the slices. Along the semi-major axis, the model overestimates the signal as it attempts to fit both sides of the asymmetric profile simultaneously. This effect is also visible across all azimuthal angles in the circular slices and persists at all radii, in line with the residuals shown earlier.

The h_4 slices reveal that, despite the larger uncertainties associated with this moment compared to the velocity and velocity dispersion maps, the model successfully reproduces the overall trend of the data. In particular, the linear slices across pointing #0 and the circular slice at small radii reveal that the rapid central decline observed in the data is well captured by the model. At larger radii, however, the intrinsic asymmetry of the data becomes evident: along the major axis, the model adjusts to the excess on the positive side (around $\sim 70°$), which in turn leads to an overestimation on the opposite side of the slice (negative semi-major axis, offset by 180°).

5.2 Viewing angles

Determining the viewing angles of M32 is crucial for linking its intrinsic and projected properties, and particularly for evaluating the possible dynamical influence of the gravitational potential of M31 on M32. In Section 3.2 of [37], the authors describe the transformation from intrinsic coordinates (x, y, z) to projected coordinates (x', y', z'). Using their Equation (10), the viewing angles (θ, ϕ, ψ) can be computed from the intrinsic shape parameters of a given model. Based on the values of (p, q, u) obtained from the parameter search (Figure 7), the corresponding viewing angles are derived and presented in Figure 10a. The full transformation consists of four rotations: the first three form a classical z–y–z sequence, expressed as $R(90°)$–$R(\theta)$–$R(\phi)$. In this framework, (θ, ϕ) describe the orientation of the intrinsic system relative to the line-of-sight direction (z'). It is interesting to highlight that the short intrinsic axis of the galaxy (z) is projected onto the y' axis (see Figure 10b). The final rotation angle, ψ, corresponds to a rotation about the line of sight, chosen such that the major axis of the innermost MGE component is aligned with the projected x' axis.

By definition, the inclination angle commonly reported in the literature corresponds to the $(i = \theta)$ angle shown in Figure 10b. Moreover, the approximate direction to M31 on the sky plane is displayed with a blue arrow. Using improved spatial coverage, higher-resolution data, and carefully calibrated astrometry and kinematics, we constructed fully triaxial models and derived viewing angles with unprecedented precision. The best-fit model (Figure 10a) gives an inclination of $\theta = 46.0^{+0.3^\circ}_{-0.5}$ (1σ) and $\theta = 46.0^{+12.5^\circ}_{-5.0}$ (3σ), significantly lower than previous estimates and with a much tighter uncertainty range. This lower inclination suggests that M32 is intrinsically flatter than previously assumed, implying a stronger role for rotational support in its dynamics.

Earlier studies provided inclination estimates but with much larger uncertainties. For instance, [39] combined SAURON and STIS kinematics under an axisymmetric assumption, excluding inclinations below 50° and finding $\theta = 70° \pm 5°$. Similarly, [36] modeled M32 as an axisymmetric system viewed nearly edge-on, reporting $\theta = 90^{+0^\circ}_{-50}$. In [38] the authors note that exploring the full inclination range would be computationally prohibitive, arguing that results would not significantly change from their adopted value of 55°. Together, these works converged on a high inclination, which our analysis now revises downward with stronger constraints.

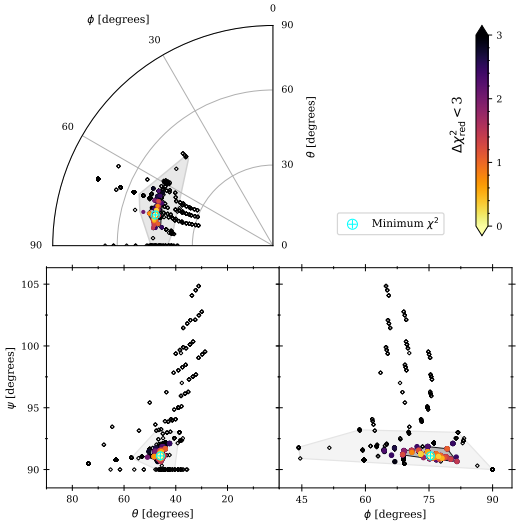

(a) Viewing angles derived from the parameter search. The angles ϕ and θ are represented on the top left graph as a sphere projection seen downwards from the North Pole. The dependency of ψ with the other two angles is shown on the graphs on the second row. The viewing angles are a result of the model and simulations, thus undergo a similar parameter search as in 7. The light and dark gray shade stand for 1σ and 3σ.

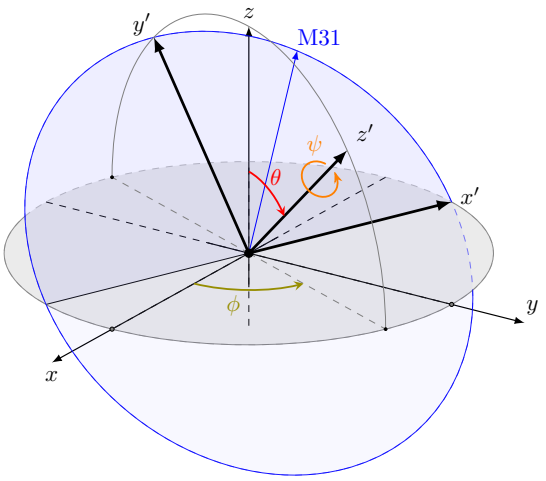

(b) Representation of the intrinsic axis of the galaxy (x, y, z) and the rotations that transform it to the sky projected plane (x', y'), perpendicular to the line of sight direction (z'). Sky projection plane shown on blue, as well as the intrinsic (x, y) plane on gray. The direction of the three angles is shown for the positive obtained values of the angles. The angle ψ is shown but yet to be applied to the coordinate system.

Figure 10: Viewing angles parameter search result and the coordinates systems rotations.

5.3 Triaxiality

After discussing the viewing angles, it is necessary to consider the intrinsic shape of the galaxy. M32 can be described as a triaxial ellipsoid with principal axes a, b, and c corresponding to the major, intermediate, and minor axes, respectively. Galaxies are commonly characterized by the axis ratios $p = b/a$ and $q = c/a$. Special cases of triaxiality include oblate axisymmetric systems, for which $p = 1$ and $q < 1$, and prolate systems, where $p \approx q < 1$. A perfectly spherical system corresponds to $p = q = 1$.

Using the parameter search results shown in Figure 7, we find best-fit intrinsic axis ratios of $(p, q) = (0.975^{+0.005}_{-0.025}, 0.44^{+0.06}_{-0.04})$ at the 1σ level and $(p, q) = \left(0.975^{+0.025}_{-0.075}, 0.44^{+0.20}_{-0.10}\right)$ at 3σ. These results confirm that M32 is close to oblate ($p \approx 1$, $T \ll 1$), but they also indicate a substantially smaller intrinsic flattening ($q = c/a$) than previously reported.

Earlier studies that assumed axisymmetry, such as [16, 38, 39], found M32 to be oblate ($p = 1$, $T = 0$) with an inclination of $i = 55°$, and [39] further reported an intrinsic flattening of $q = 0.68 \pm 0.03$. More recent work by [36], which employed triaxial models, yielded best-fit shapes close to oblate ellipsoids, with $p = 0.95 \pm 0.05$ and $q = 0.76^{+0.0}_{-0.2}$. Overall, these studies consistently converged on an interpretation of M32 as a nearly oblate system with $p \approx 1$ and moderate flattening ($q \sim 0.7$). However, the exact degree of triaxiality remained uncertain, partly because earlier works relied on axisymmetric models, and in the case of [36], the triaxial models focused primarily on constraining the central black hole mass rather than the intrinsic shape.

While the (p, q) aforementioned values provide the global shape parameters for the model and are used in the initial simulation step to deproject the MGE, the orbit-weighting procedure allows us to trace how the axis ratios of the stellar light ellipsoid evolve with radius (see Figure 11a). In the innermost region ($r < 10$ pc), the galaxy is consistent with an oblate configuration ($p = 1$, $T = 0$) with $q \sim 0.5$. At larger radii, the system becomes mildly triaxial, with $T = 0.10 \pm 0.025$ and $p = 0.97 \pm 0.01$ for 1σ. The intrinsic flattening evolves from $q \sim 0.4$ within $r < 110$ pc to $q \sim 0.6$ at larger radii. Compared to the triaxial models of [36], which were based on data of similar spatial resolution but with three times smaller spatial coverage and a much coarser instrumental resolution of $\sigma \approx 90$ km s^{-1}, the present dataset enables, once again, a more detailed characterization of the intrinsic structure of M32.

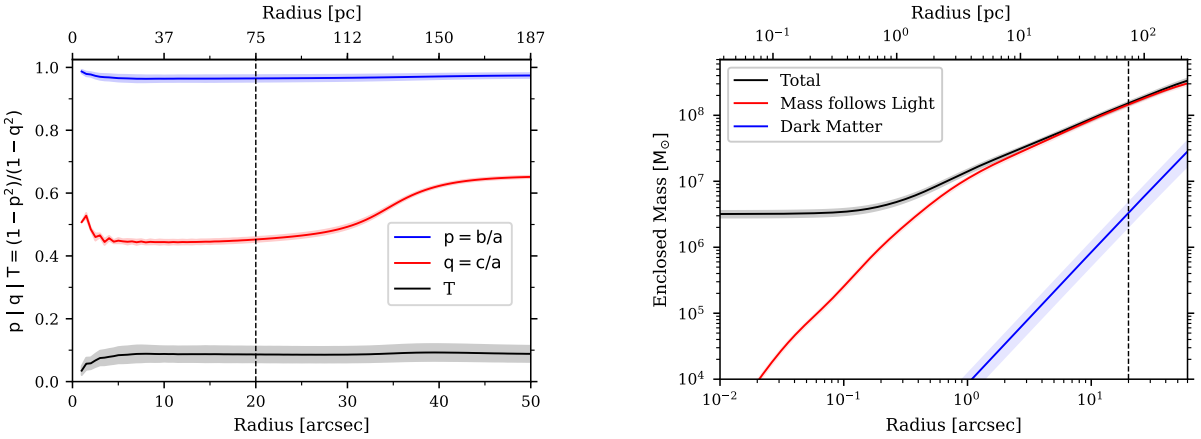

(a) Triaxiality and axis ratios for increasing radius.

(b) Mass components distribution against the radius.

Figure 11: The first graph shows the dependency of the galaxy intrinsic axis ratios and the triaxiality with the radius. The second graph represents the different mass components values for each galactocentric radius in a logarithmic scale. The total mass distribution also includes mass that does not follow light, like the central black hole. On both figures the kinematic observation limit is shown at around 20 arcsec with a dashed line. On both images, the shaded area represents the 1σ region of the error.

5.4 Supermassive central black hole

Our best-fit model, based on the parameter search in Figure 7, yields a black hole mass of $\left(3.6^{+0.2}_{-0.1}\right) \times 10^6$ $M_\odot$ (1σ), with uncertainties significantly smaller than in previous studies. The model also constrains the characteristic length scale of the black hole to $\left(3.2^{+1.2}_{-0.5}\right) \times 10^{-3}$ pc (1σ), a value orders of magnitude below the spatial resolution of the observations, justifying its modeling as a point source. The uncertainties on this length scale effectively span the full explored parameter range, as models within 1σ of the best fit exist for all sampled values of this parameter.

These results are consistent with earlier measurements: The results of [38] reported $(3.4 \pm 0.7) \times 10^6$ $M_\odot$ from axisymmetric models, while [36] obtained $(4.0 \pm 0.5) \times 10^6$ M$\odot$ for an edge-on configuration ($i = 90°$) and $(2.5 \pm 0.5) \times 10^6$ $M_\odot$ for $i = 70°$.

Figure 11b shows the enclosed mass of M32 as a function of galactocentric radius, separating the total mass, the dark matter component, and the mass that follows light. Due to the high central concentration of M32 (c-dh= 10 ± 5 at 1σ) and the limited radial extent of the data, the dark matter contribution is negligible in the innermost regions compared to the baryonic component. The difference between the luminous mass, dark mass, and total mass at the center corresponds to the supermassive black hole.

At larger radii—beyond the observed kinematic coverage—the dark matter component becomes increasingly significant in the enclosed mass profile. It is therefore expected that at sufficiently large galactocentric distances, the dark halo of M32 would dominate its gravitational potential, shaping its outer kinematics and long-term dynamical evolution. However, the radius at which this transition occurs may be so large that the gravitational influence of the much more massive halo of M31 becomes the primary driver instead.

The best-fit model yields a total stellar mass of $M_\star = 4 \times 10^8$ $M_\odot$ and a total halo mass of $M_{200} = 4 \times 10^{11}$ $M_\odot$, measured at the NFW characteristic radius $r_{200} \approx 15$ kpc (well beyond the radial range shown in Figure 11b). However, these values carry large uncertainties, as the halo parameters (c-dh and f-dh) are only weakly constrained by the parameter search shown in Figure 7. Measurements reading larger galactocentric distances would be needed in that regard.

5.5 Orbit type classification

Beyond constraining global parameters such as the viewing angles, intrinsic shape, or enclosed mass, orbit-based dynamical models also allow for a detailed investigation of the internal orbital structure of the galaxy. These models not only reproduce the observed kinematics but also disentangle the underlying stellar mo-

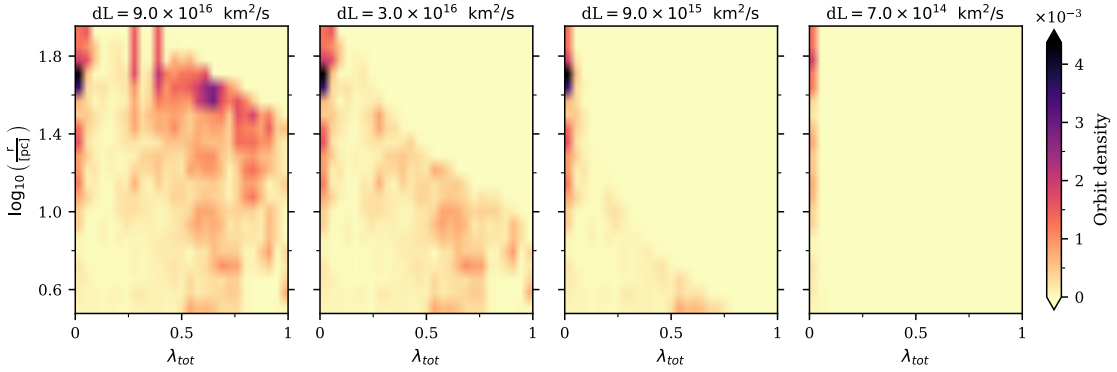

(a) Box orbit densities as a function of total normalized angular momentum and radius. From left to right, progressively smaller dL limits are applied until the $\lambda_{tot} \sim 0$ criterion is met, completing classification.

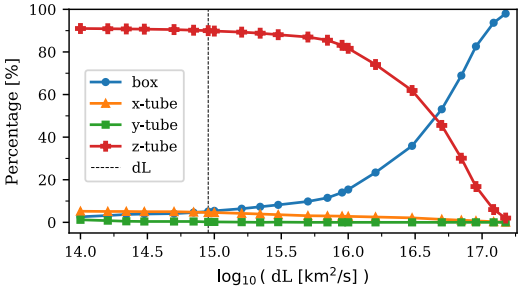

(b) Percentage variation of orbit type as a function of dL.

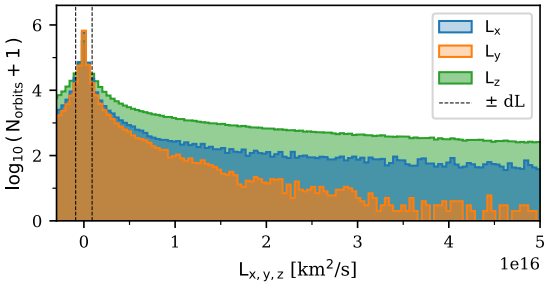

(c) Histogram of each orbit value of L_x, L_y, L_z.

Figure 12: Set of figures that represent the empirical process of determining the limit dL.

tions, showing how different families of orbits contribute to the overall dynamics. In particular, the stellar trajectories can be grouped into box orbits and tube orbits. Their relative fractions provide valuable insight into the balance between rotational support and random motions.

By definition, box orbits are characterized by an averaged angular momentum close to zero, which implies that all three components of the averaged angular momentum remain below a given threshold dL. This means that in a box orbit, every component of the averaged angular momentum is smaller than the threshold $|L_x|, |L_y|, |L_z| < dL$. Building on this, and following a similar procedure used in [40], I adopt an empirical approach to distinguish between orbit families: first, by using this threshold in L to separate box from tube orbits, and second, by classifying tube orbits according to which component of the averaged angular momentum (L_x, L_y, L_z) is dominant. It is important to note that the angular momentum components are defined with respect to the intrinsic axes of the galaxy.

Figure 12a shows the density of box orbits as a function of total averaged angular momentum and radius. Because only box orbits are plotted, increasing the value of dL naturally increases the number of orbits classified as box, including some with $\lambda_{tot} > 0$. The empirical threshold that cleanly separates box from tube orbits—ensuring that all box orbits are confined to the smallest λ_{tot} bin—is found to be $dL = 9 \times 10^{14}$ km^2/s. In Figure 12b, the fraction of each orbit family is displayed as a function of dL. The chosen empirical threshold (marked by a vertical dashed line) reveals that approximately 90% of the orbits are z-tubes, with x-tubes and box orbits each contributing around 5%, and the unstable y-tubes making up the remainder. The dependence of these fractions on the adopted dL is clearly visible and consistent with the classification scheme described above. Finally, Figure 12c presents the distribution of the individual angular momentum components. The majority of orbits exhibit relatively small values of L_y, while L_z emerges as the dominant component. These results highlight the importance of rotation around the intrinsic short axis of the galaxy, showing that M32 is strongly rotation supported. This conclusion is consistent with the lower inclination angle and higher intrinsic flattening (smaller $q = c/a$) inferred earlier, reinforcing the picture of M32 as a more flattened, disk-like system than suggested by some previous studies.

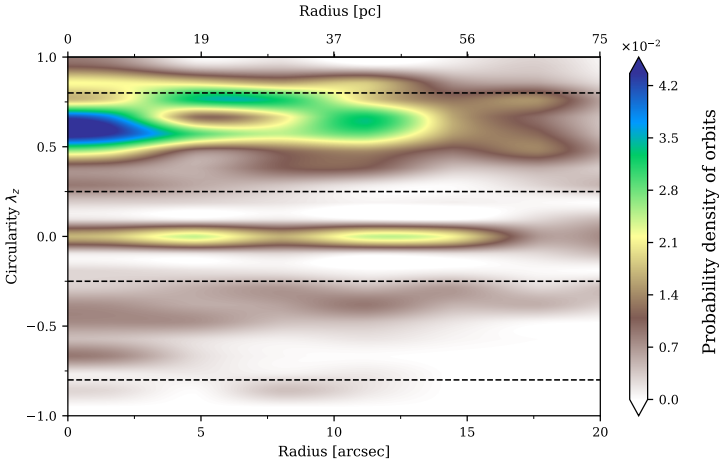

(a) Probability density of orbits as a function of circularity (λ_z) and galactocentric radius. Regions corresponding to cold, warm, and hot orbits are separated by constant λ_z thresholds, while counter-rotating orbits are those with $\lambda_z < 0$.

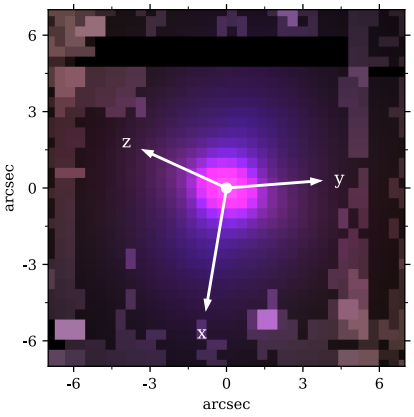

(b) Composite RGB sky projection of orbit families: long axis, intermediate axis, and box orbits shown in red, green, and blue, respectively.

Figure 13: Different visualizations of the orbital structure in M32. Left: Distribution of circularity of the short axis (λ_z) as a function of radius. Right: Projected distribution of orbit families in the central region of M32, based on the empirically derived angular momentum threshold $dL = 9 \times 10^{14}$ km^2/s. Short axis tube orbits are excluded to avoid saturation and highlight the structure of the other orbit families.

Studying how each orbital family populates the galaxy provides key insights into the dynamical state of M32 and its evolutionary history. Orbit-based dynamical models not only reproduce the observed kinematics but also reveal the orbital distribution across energy and angular momentum phase space. One powerful diagnostic in this context is the circularity parameter λ_z, defined as in [40] and [17]:

$$\lambda_z = \frac{\overline{L_z}}{r \times \overline{V_c}}. \tag{2}$$

When calculated for each orbit as a function of galactocentric radius (Figure 13a), $\lambda_z = 1$ corresponds to nearly circular *cold* orbits, $\lambda_z = 0$ indicates radial *hot* orbits, and intermediate values correspond to *warm* orbits ($0.25 \leq \lambda_z \leq 0.8$). Negative λ_z values identify counter-rotating trajectories. Orbits with $\lambda_z \approx 0$ are predominantly box orbits with near-zero average angular momentum.

In the circularity map of short-axis tube orbits, most orbits lie in the warm and cold regime, particularly at smaller radii, whereas box orbits appear as a constant density band centered near $\lambda_z = 0$. Interestingly, the best-fit model also includes a population of counter-rotating *warm* orbits ($\sim$ 15% of total orbits are counter-rotating).

Studies on larger samples such as [40], based on CALIFA, show that higher mass elliptical galaxies typically have a greater fraction of stars on *hot* and *warm* orbits, whereas less massive systems are generally more rotationally supported, with fewer stars on *hot* orbits. By contrast, M32 exhibits a higher than expected fraction of hot orbits for its mass. The elevated density of hot orbits, together with the presence of counter-rotating orbits, is consistent with a history of tidal stripping and the influence of the massive halo of M31 (see [19] for an in depth analysis of the tidal interaction between the two galaxies). Thanks to its proximity and high surface brightness, M32 provides a uniquely detailed view of compact elliptical galaxy dynamics, a regime that remains largely inaccessible for most cEs at greater distances.

Lastly, using the empirically derived threshold of $dL = 9 \times 10^{14}$ km^2/s to classify orbits, a composite RGB map of the different orbital families projected onto the sky is shown in Figure 13b. Only the most-inner part is shown as artifacts appear on regions with S/N smaller than $\sim$ 50. The intrinsic axes of the galaxy, illustrated in Figure 10b, are overlaid to highlight how the red and green long and intermediate axis tube orbits predominantly rotate about their respective axes, in contrast to the blue box orbits which, owing to

their near zero total angular momentum, populate the central regions in a more chaotic and space filling manner. As expected, intermediate-axis tube orbits are dynamically unstable and contribute negligibly to the overall orbital structure. The short axis tube orbits are excluded from this projection to prevent them from saturating the image and obscuring information about the other orbital families. As expected, intermediate axis tube orbits are dynamically unstable and contribute negligibly to the overall orbital structure.

6 Discussion and conclusion

Several formation scenarios have been proposed to explain the origin of galaxies shaped by interactions, and more specifically, of cE galaxies (such as M32). One relevant model is the "galaxy threshing" hypothesis of [3], in which a low-mass spiral galaxy is drawn into M31 and undergoes severe tidal stripping, losing its outer disk and halo while channeling gas to the center to trigger nuclear starbursts. More recent studies suggest variations on this picture: [19] argue that M32 is the stripped core of a spiral galaxy that merged with M31 roughly 2 Gyr ago, while [18] claim that tidal stripping alone cannot explain the morphology of M32, requiring an intrinsically compact progenitor. In all cases, tidal interactions with M31 are expected to leave dynamical relics, such as counter-rotation and nuclear disks, which can now be tested against high-quality integral-field data.

Our dynamical models of M32 provide a new observational perspective on these scenarios. The best-fit Schwarzschild model constrains the central SMBH mass to $\left(3.6^{+0.2}_{-0.1}\right) \times 10^6$ $M_\odot$, consistent with earlier estimates from HST and SAURON [36, 38, 39] but with significantly tighter uncertainties thanks to the higher spatial resolution and spectral coverage of MEGARA. This mass is remarkably similar to that of the SMBH of the Milky Way, despite the large difference in host galaxy mass and morphology, indicating that either SMBHs can grow in very different galaxies or that the cEs can indeed be deprived of a large fraction of its stellar content due to close interactions and might have suffered major structural transformations in the process.

We also find that M32 is viewed at a lower inclination ($\theta = 46.0^{+0.3^\circ}_{-0.5}$) than previously assumed, implying that it is intrinsically flatter, with a short to long axis ratio for deprojection of $q = 0.44^{+0.06}_{-0.04}$. Flatter systems are typically more rotationally supported, and our orbital decomposition indeed reveals that rotation contributes significantly to the dynamics of M32—with around 90% of orbits as tubes around the short axis. The radial variation of axis ratios and triaxiality further suggests the presence of an embedded nuclear disk. These features are consistent with gas inflows and central star formation during past interactions, as envisioned in interaction-driven scenarios.

The orbit classification we did showed that $\sim 15\%$ of stars occupy hot ($\lambda_z \sim 0$) orbits and another $\sim 15\%$ counter-rotating ($\lambda_z < 0$) orbits. Such orbital components provide direct dynamical evidence of tidal interactions, which redistribute angular momentum and favor counter-rotation orbit generation. Their presence strengthens the case that the observable kinematics of M32 were shaped not only by intrinsic prior compactness but also by nurture through encounters with M31.

Discrepancies with earlier studies—like the already mentioned [36, 39, 38]—can largely be attributed to differences in spatial resolution and coverage. SAURON-based analyses, for instance, focused on smaller galactocentric radii and likely missed the intrinsically flatter inner disk component that we recover here. Our coverage out to ~ 70 pc around the center of M32, combined with the spectral resolution of MEGARA, provides the most complete dynamical view of the central structure of M32 to date.

Taken together, these results show that M32 is not a simple pressure-supported spheroid, but rather a rotationally supported, flattened system bearing clear signatures of tidal interaction. Its SMBH mass, intrinsic shape, and orbital decomposition are all consistent with a history in which both stripping and gas inflow shaped its current state.

Looking ahead, combining dynamical modeling with stellar population analysis—such as the ongoing development of `DYNAMITE`—will make it possible to connect dynamically distinct orbit families with specific star formation episodes. This will clarify whether the counter-rotating and nuclear disk components correspond to populations formed during interaction-induced bursts, or to older stars dynamically restructured by tidal forces. Such work will be key to fully reconstructing the evolutionary pathway of M32 and to understanding cE galaxies as a class.

In conclusion, our study provides the most detailed orbital decomposition of a cE galaxy to date. High-

resolution MEGARA spectroscopy, combined with Schwarzschild modeling, refines the SMBH mass of M32, reveals its intrinsic flattening and rotational support, and uncovers orbital evidence of tidal interactions. These results support interaction-driven formation scenarios and underscore the relation between internal galaxy structure with environmental processes and the formation of cE galaxies.

A Appendix I. Kinematic pointing calibration implementation

See the Section here: Google Drive link of Appendix A.

B Appendix II. Simulation results after imposing symmetry on h3 kinematic map

In this Appendix we impose symmetry on the h_3 kinematic map by applying a uniform correction—equal to the mean value of the third kinematic calibration method h_3 map—across the entire field. The corrected data maps then undergo a short parameter search, similar to that shown in Figure 7. In this case, ~ 50 models were integrated. The best-fit result of this search is presented in Figures 14 and 15 (see link to external file for Figures in this Appendix). Following the workflow described in Section 3.3.2, this procedure can be considered a fourth calibration method: method three plus the imposition of h_3 symmetry.

At first glance, the resulting kinematic maps do not differ significantly from those of the previous simulations (Figures 8 and 9). The main improvement lies in the error map of the h_3 GH moment, which is smaller and closer to zero compared to the non-symmetric h_3 models. As discussed in Section 5.1, Schwarzschild models inherently return symmetric outputs, which naturally provide a better fit to symmetrized data. The larger residuals seen in the central region of the h_3 map are caused, as with the velocity map, by the very small observational uncertainties as the model cannot perfectly reproduce all features across all kinematic moments simultaneously.

Overall, although the kinematic maps appear visually similar to those of the third method, the fit quality is much improved when using symmetrized data. The best-fit model yields a significantly smaller $\chi^2_{\rm red}$ than in the non-symmetric case ($\chi^2_{\rm red} = 2.7$ with the imposed symmetry). Nevertheless, the internal dynamical properties remain essentially unchanged: the (p, q, T) shape parameters, enclosed mass profile, and circularity distribution all agree within 1σ of the third method (see Section 5). Even the orbit-type fractions are virtually identical.

The only prominent discrepancy between the best-fit model and the data appears in the SE region of the h_4 map, corresponding to pointings #7 and #8. This mismatch arises from the model enforcing symmetry, whereas the data display an intrinsic asymmetry.

One might argue that, in analogy with h_3, the h_4 map could also be symmetrized. However, this correction is not straightforward. The h_3 asymmetry corresponded to a uniform shift across the map, plausibly linked to calibration issues. In contrast, the h_4 deviations appear localized. There is a h_4 excess along the positive major axis present in pointings #0, #3, and #4. Their spatial coherence across different pointings suggests a possible physical origin in M32 rather than a calibration artifact. Potential explanations include contamination from the M31 disk, stars from the outer regions of the halo of M32, or tidal interaction signatures. A detailed stellar population analysis with `DYNAMITE` could provide further insight.

See the Figures here: Google Drive link of Figures of Appendix B.

References

[1] Andrae, R., Schulze-Hartung, T., & Melchior, P. 2010, arXiv e-prints, arXiv:1012.3754, doi: 10.48550/arXiv.1012.3754

[2] Avni, Y. 1976, ApJ, 210, 642, doi: 10.1086/154870

[3] Bekki, K., Couch, W. J., Drinkwater, M. J., & Gregg, M. D. 2001, ApJ, 557, L39, doi: 10.1086/323075

[4] Bryant, J. J., Owers, M. S., Robotham, A. S. G., et al. 2015, MNRAS, 447, 2857, doi: 10.1093/mnras/stu2635

[5] Bundy, K., Bershady, M. A., Law, D. R., et al. 2015, ApJ, 798, 7, doi: 10.1088/0004-637X/798/1/7

[6] Cappellari, M. 2002, MNRAS, 333, 400, doi: 10.1046/j.1365-8711.2002.05412.x

[7] Cappellari, M. 2017, Monthly Notices of the Royal Astronomical Society, 466, 798, doi: 10.1093/mnras/stw3020

[8] Cappellari, M. 2023, MNRAS, 526, 3273, doi: 10.1093/mnras/stad2597

[9] Cappellari, M., & Emsellem, E. 2004, PASP, 116, 138, doi: 10.1086/381875

[10] Cappellari, M., Emsellem, E., Krajnović, D., et al. 2011, MNRAS, 413, 813, doi: 10.1111/j.1365-2966.2010.18174.x

[11] Castillo Morales, A., Pascual, S., & Gil de Paz, A. 2020, MEGARA Data Reduction Cookbook, Software documentation, Universidad Complutense de Madrid; published via Zenodo, doi: 10.5281/zenodo.3834345

[12] Chamorro-Cazorla, M., Gil de Paz, A., Castillo-Morales, Á., et al. 2023, A&A, 670, A117, doi: 10.1051/0004-6361/202245111

[13] Choi, P. I., Guhathakurta, P., & Johnston, K. V. 2002, AJ, 124, 310, doi: 10.1086/341041

[14] Coelho, P. 2014, MNRAS, 440, 1027, doi: 10.1093/mnras/stu365

[15] Conroy, C. 2013, ARA&A, 51, 393, doi: 10.1146/annurev-astro-082812-141017

[16] Dehnen, W. 1995, Monthly Notices of the Royal Astronomical Society, 274, 919, doi: 10.1093/mnras/274.3.919

[17] denBrok, M., Krajnović, D., Emsellem, E., Brinchmann, J., & Maseda, M. 2021, Monthly Notices of the Royal Astronomical Society, 508, 4786, doi: 10.1093/mnras/stab2852

[18] Dierickx, M., Blecha, L., & Loeb, A. 2014, ApJ, 788, L38, doi: 10.1088/2041-8205/788/2/L38

[19] D'Souza, R., & Bell, E. F. 2018, Nature Astronomy, 2, 737, doi: 10.1038/s41550-018-0533-x

[20] Emsellem, E., Monnet, G., & Bacon, R. 1994, A&A, 285, 723

[21] Gil de Paz, A., Carrasco, E., Gallego, J., et al. 2018, in Ground-based and Airborne Instrumentation for Astronomy VII, ed. C. J. Evans, L. Simard, & H. Takami, Vol. 10702, International Society for Optics and Photonics (SPIE), 1070217, doi: 10.1117/12.2313299

[22] Jethwa, P., Thater, S., Maindl, T., & van de Ven, G. 2025, Dynamite (DYnamics, Age and Metallicity Indicators Tracing Evolution), https://github.com/dynamics-of-stellar-systems/dynamite, GitHub

[23] Karachentsev, I. D., & Kashibadze, O. G. 2006, Astrophysics, 49, 3, doi: 10.1007/s10511-006-0002-6

[24] Kent, S. M. 1987, AJ, 94, 306, doi: 10.1086/114472

[25] Ma, C.-P., Greene, J. E., McConnell, N., et al. 2014, The Astrophysical Journal, 795, 158, doi: 10.1088/0004-637X/795/2/158

[26] Michard, R., & Nieto, J. L. 1991, A&A, 243, L17

[27] NASA/IPAC Extragalactic Database (NED). 2025, NASA/IPAC Extragalactic Database, https://ned.ipac.caltech.edu/

[28] Pascual, S., Cardiel, N., Gil de Paz, A., et al. 2019, in Highlights on Spanish Astrophysics X, ed. B. Montesinos, A. Asensio Ramos, F. Buitrago, R. Schödel, E. Villaver, S. Pérez-Hoyos, & I. Ordóñez-Etxeberria, 227–227

[29] Sánchez, S. F., Kennicutt, R. C., Gil de Paz, A., et al. 2012, A&A, 538, A8, doi: 10.1051/0004-6361/201117353

[30] Sanchez-Blazquez, P., Peletier, R. F., Jimenez-Vicente, J., et al. 2006, Monthly Notices of the Royal Astronomical Society, 371, 703–718, doi: 10.1111/j.1365-2966.2006.10699.x

[31] Santucci, G., Brough, S., van de Sande, J., et al. 2022, The Astrophysical Journal, 930, 153, doi: 10.3847/1538-4357/ac5bd5

[32] Schwarzschild, M. 1979, ApJ, 232, 236, doi: 10.1086/157282

[33] Space Telescope Science Institute. 2025, Hubble Space Telescope Documentation, https://www.stsci.edu/hst/documentation

[34] Tinsley, B. M. 1980, Fund. Cosmic Phys., 5, 287, doi: 10.48550/arXiv.2203.02041

[35] van de Sande, J., Bland-Hawthorn, J., Fogarty, L. M. R., et al. 2017, ApJ, 835, 104, doi: 10.3847/1538-4357/835/1/104

[36] van den Bosch, R. C. E., & de Zeeuw, P. T. 2010, MNRAS, 401, 1770, doi: 10.1111/j.1365-2966.2009.15832.x

[37] van den Bosch, R. C. E., van de Ven, G., Verolme, E. K., Cappellari, M., & de Zeeuw, P. T. 2008, MNRAS, 385, 647, doi: 10.1111/j.1365-2966.2008.12874.x

[38] van der Marel, R. P., de Zeeuw, P. T., Rix, H.-W., & Quinlan, G. D. 1997, Nature, 385, 610, doi: 10.1038/385610a0

[39] Verolme, E. K., Cappellari, M., Copin, Y., et al. 2002, Monthly Notices of the Royal Astronomical Society, 335, 517, doi: 10.1046/j.1365-8711.2002.05664.x

[40] Zhu, L., van de Ven, G., van den Bosch, R., et al. 2018, Nature Astronomy, 2, 233, doi: 10.1038/s41550-017-0348-1